Influences of the Sierra Nevada on Intermountain Cold-Front Evolution

GREGORY L. WEST

Department of Earth and Ocean Sciences, University of British Columbia, and BC Hydro Corporation, Vancouver, British Columbia, Canada

W. JAMES STEENBURGH

Department of Atmospheric Sciences, University of Utah, Salt Lake City, Utah

(Manuscript received 10 December 2010, in final form 25 May 2011)

ABSTRACT

Recent studies indicate that strong cold fronts develop frequently downstream of the Sierra Nevada over the Intermountain West. To help ascertain why, this paper examines the influence of the Sierra Nevada on the rapidly developing Intermountain cold front of 25 March 2006. Comparison of a Weather Research and Forecasting (WRF) model control simulation with a simulation in which the height of the Sierra Nevada is restricted to 1500 m (roughly the elevation of the valleys and basins of the Intermountain West) shows that the interaction of southwesterly prefrontal flow with the formidable southern High Sierra produces a leeward orographic warm anomaly that enhances the cross-front temperature contrast. Several processes generate this orographic warm anomaly, including flow modification by the Sierra Nevada (i.e., windward blocking of low-level Pacific air, leeward subsidence, and increased southerly flow from the Mojave Desert and lower Colorado River basin into the Intermountain West), diabatic heating and water vapor loss associated with orographic precipitation, and increased sensible heating and reduced subcloud diabatic cooling in the downstream cloud and precipitation shadow. In contrast, the postfrontal air mass experiences comparatively little orographic modification as it moves across the relatively low northern Sierra Nevada. These results show that the Sierra Nevada can enhance frontal development, which may contribute to the high frequency of strong cold-frontal passages over the Intermountain West.

1. Introduction

The topographically complex western United States is a region where mountains play a major role in frontal evolution (e.g., Braun et al. 1997; Colle et al. 1999; Steenburgh and Blazek 2001; Colle et al. 2002; Shafer et al. 2006; Shafer and Steenburgh 2008; Steenburgh et al. 2009). As cold fronts approach the Pacific coast, orographic blocking and friction produce enhanced prefrontal southerly flow, confluent deformation, frontogenesis, frontal deceleration, and, in some cases, a barrier jet (e.g., Braun et al. 1997; Doyle 1997; Colle et al. 1999; Yu and Smull 2000; Neiman et al. 2002, 2004, 2010). Colle et al. (2002) illustrate these topographic effects with a model sensitivity study in which coastal topography is removed, which results in a weaker, more progressive cold front.

Farther downstream, recent observational and modeling studies document several manifestations of front–mountain interactions over the Intermountain West (see Fig. 1 for geographic references). These interactions include orographic blocking and frontal retardation windward of the Sierra Nevada (Steenburgh and Blazek 2001; Shafer et al. 2006), discrete frontal propagation across the Sierra–Cascade ranges and Intermountain West (Steenburgh et al. 2009), and frontal distortions produced by basin-and-range and other topographic geometries (Steenburgh and Blazek 2001; West and Steenburgh 2010). In addition, West and Steenburgh (2010) describe how the Great Basin confluence zone (GBCZ), an area of confluent deformation and convergence that develops downstream of the Sierra Nevada, can serve as a locus for frontal development.

None of these studies have used numerical sensitivity experiments to examine the role of the Sierra Nevada in

Corresponding author address: Dr. W. James Steenburgh, Dept. of Atmospheric Sciences, University of Utah, Rm. 819, 135 South 1460 East, Salt Lake City, UT 84112.
E-mail: jim.steenburgh@utah.edu

DOI: 10.1175/MWR-D-10-05076.1

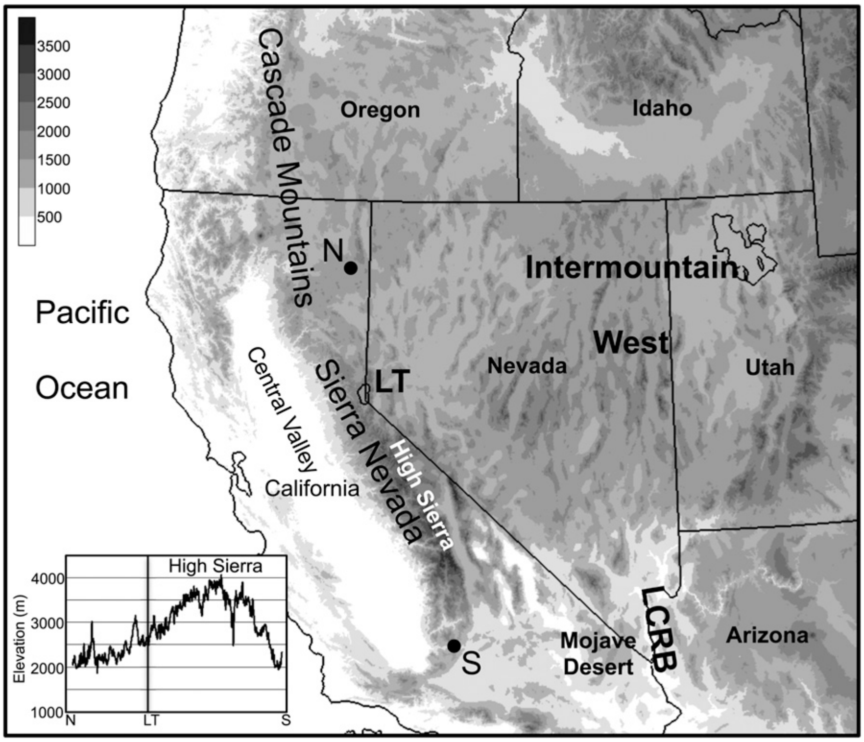

FIG. 1. The 30-s mean topography (m, shaded following scale at upper left) of the Intermountain West and adjoining regions, with the height of the Sierra Nevada crest between points N and S at lower left (position of Lake Tahoe indicated by vertical line). Abbreviations are used for Lake Tahoe (LT) and the lower Colorado River basin (LCRB).

Intermountain cold-front evolution. Oriented from north-northwest to south-southeast, the Sierra Nevada occupy most of eastern California and join the Cascade Mountains in northern California (Fig. 1). The crest of the Sierra–Cascade ranges is relatively low north of Lake Tahoe, but reaches altitudes of more than 3500 m in the southern High Sierra south of Lake Tahoe (Fig. 1, inset). The Sierra Nevada generate orographic clouds and precipitation (e.g., Varney 1920; Lee 1987; Rauber 1992; Galewsky and Sobel 2005; Reeves et al. 2008; Lundquist et al. 2010; Smith et al. 2010), as well as leeward subsidence and cloud and precipitation shadowing (e.g., Varney 1920; Smith et al. 1979; Jiang and Doyle 2008). Studies of front–mountain interactions in other parts of the world show that prefrontal warming produced during flow over topography (i.e., from diabatic heating in the orographic cloud and leeward subsidence) can be frontogenetical and increase the cross-front temperature contrast (e.g., Shapiro 1984; Kurz 1990; Hoinka and Volkert 1992; Colle et al. 1999, Neiman et al. 2001). Recent studies over the Intermountain West suggest that flow interactions with the Sierra Nevada, especially the High Sierra, contribute to the development of the GBCZ, frontal intensification over Nevada, and the high frequency of strong cold-frontal passages over the region (Shafer and Steenburgh 2008; Steenburgh et al. 2009; West and Steenburgh 2010).

Here, we examine how the Sierra Nevada contribute to the development and strength of the Intermountain cold front of 25 March 2006, which propagated discretely across the northern Sierra Nevada and southern Cascade Mountains [see Steenburgh et al. (2009) for a detailed analysis], intensified rapidly over Nevada (Fig. 2), and produced the sixth largest temperature change in the 25-yr cold-front climatology of Shafer and Steenburgh (2008). Of particular interest is determining how the Sierra Nevada modify the pre- and postfrontal air masses and resulting frontal evolution. Our approach involves comparing a full-terrain control simulation by the Weather Research and Forecasting (WRF) model with a simulation in which the height of the Sierra Nevada is restricted to 1500 m, roughly the elevation of the valleys and basins of the Intermountain West. Analysis of the two simulations shows that the interaction of prefrontal southwesterly flow with the southern High Sierra produces a leeward orographic warm anomaly that enhances the cross-front temperature contrast, but has little influence on the discrete propagation or frontal positioning.

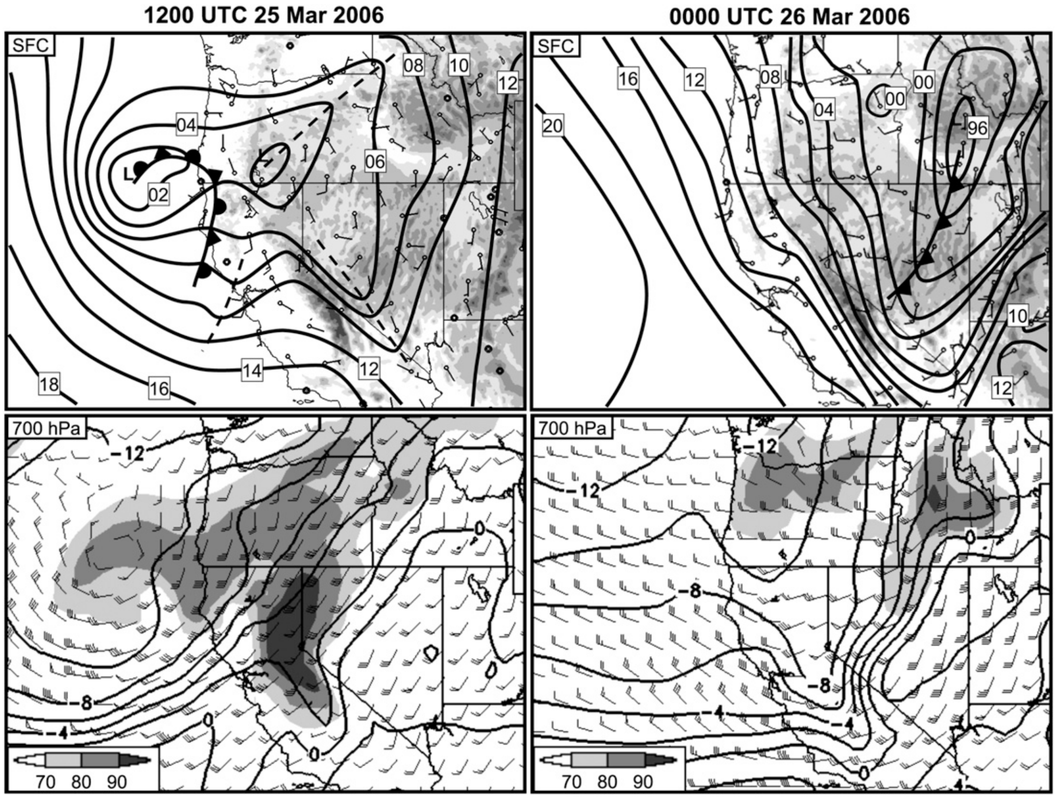

FIG. 2. Synoptic structure of the 25 Mar 2006 cold front at (left) 1200 UTC 25 Mar and (right) 0000 UTC 26 Mar 2006. (top) Manual surface analyses include conventional frontal symbols, sea level contours (every 2 hPa), and surface wind observations (full and half barb denote 5 and 2.5 m s^{-1}, respectively). (bottom) NAM 700-hPa analyses include temperature contours (every 2°C), wind (full and half barb denote 5 and 2.5 m s^{-1}, respectively), and 800–500-mb mean relative humidity (%, shaded following scale at lower left). [Adapted from Steenburgh et al. (2009).]

2. Data and methods

All simulations of the 25 March 2006 cold front use the Advanced Research core of the Weather Research and Forecasting (WRF) model, version 2.2.1 (Skamarock et al. 2005). The full-terrain control simulation (FULLTER) is identical to the control (CTL) run described by Steenburgh et al. (2009), and features a 36-km outer domain, 12-km inner nest (the only domain presented in this paper), 34 half-η levels in the vertical, and unaltered topography (Fig. 3a). Physics packages include the Rapid Radiative Transfer Model (RRTM) longwave radiation parameterization (Mlawer et al. 1997), the Dudhia shortwave radiation parameterization (Dudhia 1989), the Noah land surface model (Chen and Dudhia 2001), the Mellor–Yamada–Janjić planetary boundary layer parameterization (Mellor and Yamada 1982; Janjić 2002), the new Kain–Fritsch cumulus parameterization [a modified version of the parameterization described by Kain and Fritsch (1990, 1993)], and the Thompson et al. (2004, 2006) microphysical parameterization. North American Mesoscale (NAM) model analyses provide the cold-start atmospheric and land surface (e.g., soil temperature, soil moisture, snow cover) initial conditions at 0000 UTC 25 March 2006 and lateral boundary conditions through the integration period, with some modifications to the lower-troposphere and the land surface analysis as described in Steenburgh et al. (2009). As discussed in Steenburgh et al. (2009), FULLTER (their CTL) captures the discrete propagation and rapid frontal development quite well, but the front advances across eastern Nevada 2–3 h faster than observed and the prefrontal boundary layer is 2°–3°C too cool during the afternoon, as compared to observations.

The NOSIERRA simulation is identical to FULLTER except that we restrict the height of the Sierra Nevada and southern Cascades of California to an elevation of 1500 m, the approximate mean elevation of the valleys and basins of the Intermountain West, prior to terrain smoothing by the WRF Preprocessing System (Fig. 3b). The resulting terrain height differences are relatively small over the northern Sierra Nevada and southern

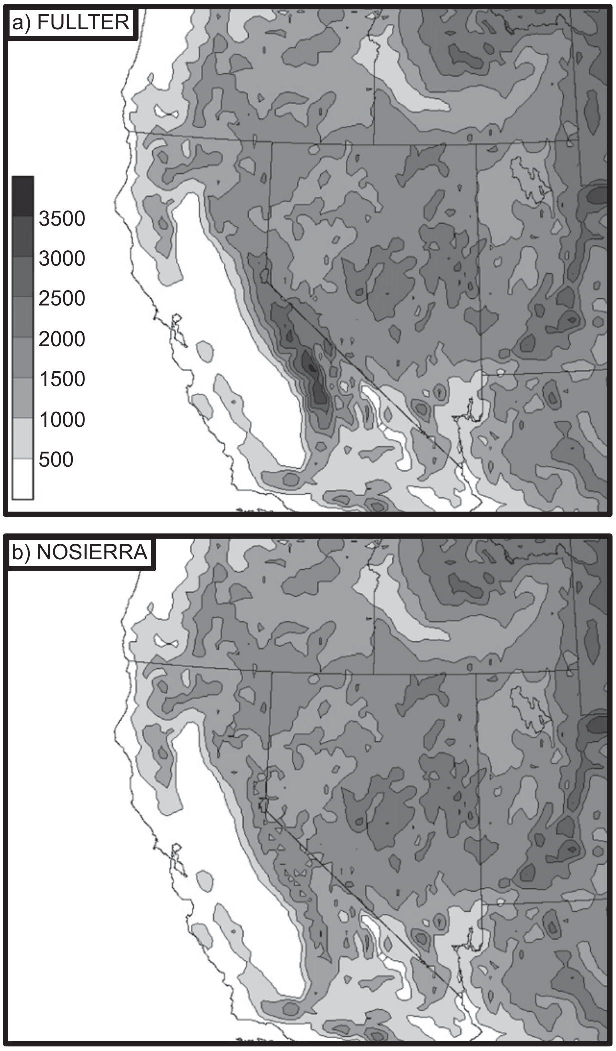

FIG. 3. WRF topography [m, shaded following scale in (a)] for a subset of the (a) FULLTER and (b) NOSIERRA 12-km nested domains.

Cascades, but much larger south of Lake Tahoe along the High Sierra. The atmosphere in the volume previously occupied by topography is derived from NAM model initial analyses or, at levels below the NAM model surface, assumes a dry-adiabatic lapse rate and uses winds from the lowest above-ground model level. Given the small topographic volume removed and the 15-h integration time before incipient frontal development, results are likely insensitive to these prescribed initial conditions. Fake-dry (FKDRY) simulations based on FULLTER or NOSIERRA topography do not include diabatic heating and cooling associated with cloud and precipitation processes. They do, however, allow simulated clouds and precipitation to interact with other model physics packages, such as the radiation parameterizations.

For figure clarity, all horizontal contour and color-fill analyses of geopotential height, potential temperature, potential-temperature gradient magnitude, frontogenesis, and potential-temperature difference between simulations are smoothed using a seven-point cowbell spectral filter (Barnes et al. 1996). This enables a clearer presentation without eliminating the mesoscale terrain signal. The 850-hPa geopotential height analysis is based on hydrostatic extrapolation where that pressure level is below the model terrain. Frontogenesis analyses may differ slightly from those in Steenburgh et al. (2009) due to a minor adjustment to the spatial differencing to better account for grid staggering.

We use several diagnostic quantities to examine the mechanisms responsible for frontal development. As in Steenburgh et al. (2009), surface frontogenesis is defined following Petterssen (1936) and Miller (1948) as

$$F = \frac{d}{dt}|\nabla_\eta \theta|, \tag{1}$$

where

$$\frac{d}{dt} = \frac{\partial}{\partial t} + u\frac{\partial}{\partial x_\eta} + v\frac{\partial}{\partial y_\eta} + \dot{\eta}\frac{\partial}{\partial \eta}, \tag{2}$$

$$\nabla_\eta = \mathbf{i}\frac{\partial}{\partial x_\eta} + \mathbf{j}\frac{\partial}{\partial y_\eta}, \tag{3}$$

the subscript η denotes differentiation along the terrain following lowest-η level, and $\dot{\eta}$ is the η-coordinate vertical velocity. Following Miller (1948), Eq. (1) may be written as

$$F = F_W + F_T + F_D, \tag{4}$$

where

$$F_W = -\frac{1}{|\nabla_\eta \theta|}\left[\frac{\partial \theta}{\partial x}\left(\frac{\partial u}{\partial x}\frac{\partial \theta}{\partial x} + \frac{\partial u}{\partial y}\frac{\partial \theta}{\partial y}\right) + \frac{\partial \theta}{\partial y}\left(\frac{\partial v}{\partial x}\frac{\partial \theta}{\partial x} + \frac{\partial v}{\partial y}\frac{\partial \theta}{\partial y}\right)\right], \tag{5}$$

$$F_T = -\frac{1}{|\nabla_\eta \theta|}\left[\frac{\partial \theta}{\partial \eta}\left(\frac{\partial \dot{\eta}}{\partial x}\frac{\partial \theta}{\partial x} + \frac{\partial \dot{\eta}}{\partial y}\frac{\partial \theta}{\partial y}\right)\right], \tag{6}$$

$$F_D = -\frac{1}{|\nabla_\eta \theta|}\left[-\frac{\partial \theta}{\partial x}\frac{\partial}{\partial x}\frac{d\theta}{dt} - \frac{\partial \theta}{\partial y}\frac{\partial}{\partial y}\frac{d\theta}{dt}\right], \tag{7}$$

and the subscript η has been dropped for convenience. Here, F_W, F_T, and F_D are the frontogenesis components produced by horizontal deformation and divergence (hereafter *kinematic frontogenesis*), tilting, and horizontal gradients in diabatic heating and cooling (hereafter *diabatic frontogenesis*), respectively. Although F_T is nonzero due to the presence of a surface-based stable layer in the morning and a superadiabatic layer in the afternoon, it does not appear to contribute significantly to frontal development and is not presented. The F_D component is calculated directly from heating rates obtained from the WRF model boundary layer, radiation, microphysical, and cumulus parameterizations.

Trajectory calculations follow Petterssen (1956, p. 27) and Seaman (1987), use three-dimensional WRF model instantaneous horizontal winds and vertical velocities, and are constrained to remain on the lowest-η level if they approach the model surface. Heating rates from the boundary layer, radiation (long- and shortwave), cumulus, and microphysical parameterizations are used to examine diabatic potential temperature changes along trajectories. We refer to the sum of the boundary layer and radiation heating rates as simply the *boundary layer heating* and *cooling* (depending on sign) since the former dominate and, for simplicity, do not distinguish between the cumulus and microphysical heating rates.

3. Results

The 25 March 2006 cold front developed rapidly over the Intermountain West (Fig. 2). Steenburgh et al. (2009) provide a thorough analysis of the event, including validation of FULLTER (their CTL). Here, we concentrate on the influence of the Sierra Nevada by comparing FULLTER and NOSIERRA.

a. Antecedent conditions

At 1500 UTC 25 March 2006, a weakening occluded front moves inland across the northern California coast, its position virtually identical in FULLTER and NOSIERRA (cf. Figs. 4a and 4b). Ahead of the occluded front, confluent south-southwesterly large-scale flow develops over northwest Nevada, initiating Intermountain cold-front development. In FULLTER, the Sierra Nevada disrupt the confluent flow, producing two weak troughs (dashed lines) and an airstream boundary (dotted line) that separates south-southeasterly flow over southern and central Nevada from southwesterly flow over northwest Nevada [Fig. 4c; see Steenburgh et al. (2009) for further discussion of these features]. In contrast, NOSIERRA produces a single trough and wind shift (Fig. 4d). FULLTER also generates more spatial variability in potential temperature over northwest Nevada (cf. Figs. 4c and 4d), although differences between the two simulations are less than 2 K (Fig. 5a).

More substantive differences are found over the southern High Sierra where the crest-height difference between the two simulations is larger (cf. Figs. 3a and 3b). In particular, FULLTER produces stronger windward ridging and lee troughing across the High Sierra (cf. Figs. 4a and 4b), southeasterly–southerly rather than southerly–southwesterly flow downstream (cf. Figs. 4c and 4d), and a broad region of higher (2–5 K) potential temperature over central Nevada that we refer to as the *orographic warm anomaly* (Fig. 5a). The aforementioned airstream boundary (dotted line) lies near the northern edge of the southeasterly–southerly flow and the orographic warm anomaly, which develops early in the simulation and spreads outward across the Intermountain West from the lee of the High Sierra.

Comparison of FULLTER and NOSIERRA cross sections taken across the High Sierra and central Nevada illustrate the vertical structure of the orographic warm anomaly at 1500 UTC (Fig. 6; see Figs. 4c, 4d, and 5 for cross-section location). The orographic warm anomaly is deepest near the Sierra Nevada but extends several hundred kilometers downstream below ~650 hPa (Fig. 6c). The Sierra Nevada produce a high-amplitude mountain wave with strong leeside subsidence in FULLTER, whereas cooler Pacific air penetrates directly into the Intermountain West in NOSIERRA (cf. Figs. 6a and 6b; cf. the fate of the 292–296-K air). As a result, a pronounced low-level cloud and precipitation shadow extends downstream from the Sierra Nevada in FULLTER, whereas precipitation and the related low-level diabatic cooling are more widespread over the Intermountain West in NOSIERRA (cf. Figs. 4a,b and Figs. 6a,b).

In addition, a more substantive orographic cloud and precipitation region exists in FULLTER compared to NOSIERRA (cf. Figs. 4a,b and 6a,b). This orographic cloud and precipitation region developed over the High Sierra after 0900 UTC and contributes to *airmass transformation* [i.e., the across-barrier loss of water content and change in potential temperature due to orographic precipitation and latent heating (e.g., Varney 1920; Giorgi and Bates 1989; Sinclair 1994; Smith et al. 2003; Smith et al. 2005)] in FULLTER.

Also during this period, confluence and convergence begin to concentrate the baroclinicity over northwest Nevada. Kinematic frontogenesis over northwest Nevada is broken into three bands along the aforementioned troughs and airstream boundary in FULLTER, but found solely along the single trough in NOSIERRA (cf. Figs. 4c and 4d). The baroclinicity is also less organized and concentrated in FULLTER compared to NOSIERRA. Nevertheless, because of the orographic warm anomaly (Fig. 5a), a larger total temperature contrast exists across northwestern Nevada in FULLTER (288–298 K) than NOSIERRA (288–292 K). At this time, diabatic frontogenesis is weak and disorganized over northwest Nevada

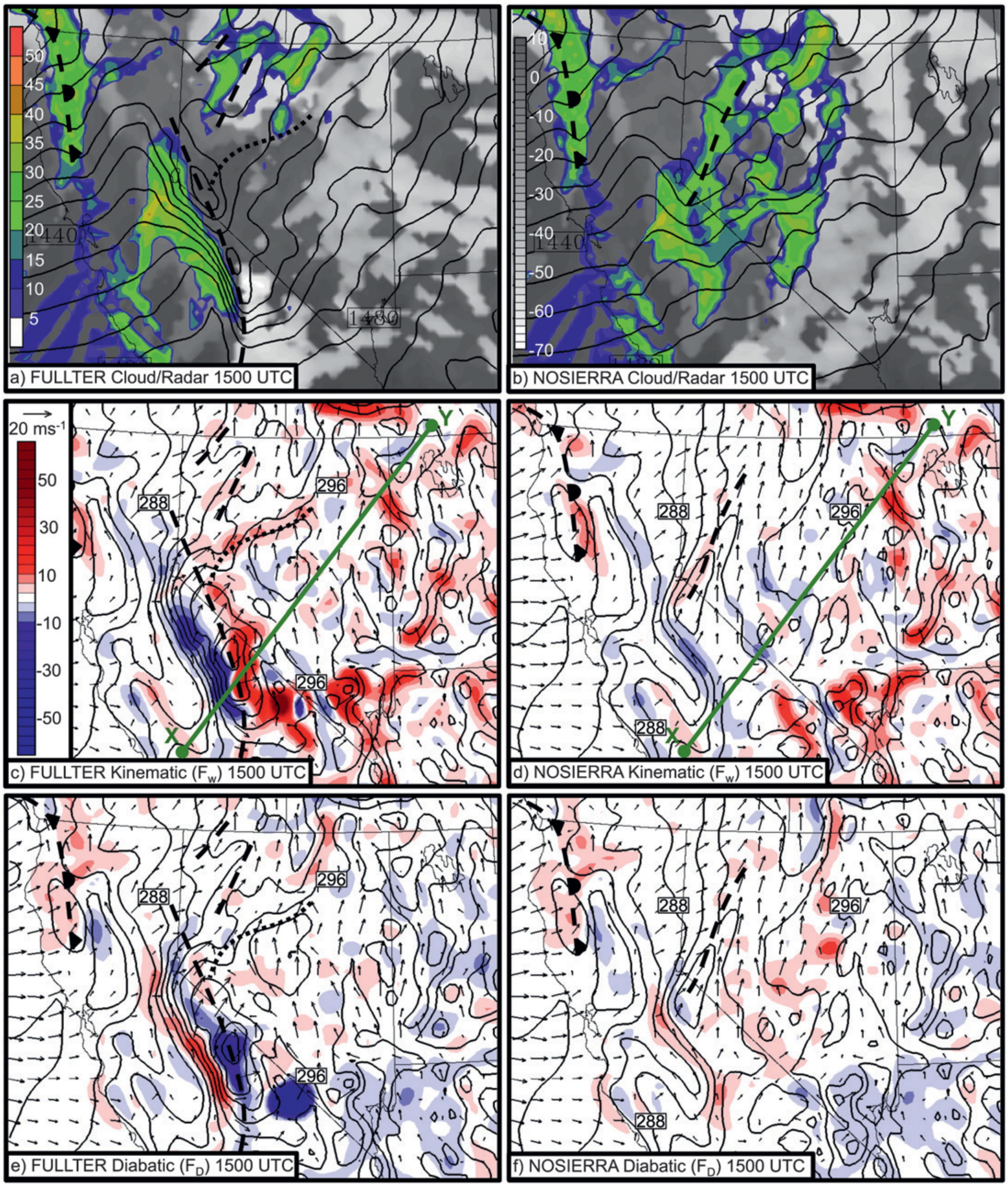

FIG. 4. WRF model analyses for 1500 UTC 25 Mar 2006 with fronts and synoptic features discussed in the text annotated. (a) FULLTER radar reflectivity [dBZ, color shaded according to scale in (a)], cloud-top temperature (°C, gray shaded according to scale in (b)], and 850-hPa geopotential height (solid contours every 10 m). (b) As in (a), but for NOSIERRA. (c) FULLTER lowest half-η-level potential temperature (contours every 2 K), wind (vector scale at left), and kinematic frontogenesis [K (100 km h)$^{-1}$, shaded following scale at left]. (d) As in (c), but for NOSIERRA. (e) As in (c), but with diabatic frontogenesis. (f) As in (e), but for NOSIERRA.

in FULLTER and weak but generally positive near the trough in NOSIERRA (Figs. 4e and 4f).

b. *Trajectory analysis of the orographic warm anomaly at 1500 UTC*

Fifteen-hour (0000–1500 UTC) three-dimensional trajectories show how flow interaction with the Sierra Nevada contributes to the development of the orographic warm anomaly at 1500 UTC (Fig. 7). We illustrate this flow interaction with forward trajectories that begin at 850 hPa in a line parallel to and upstream of the Sierra Nevada (group X, brown) and backward trajectories that end at 850 hPa (or the lowest-η level if the model terrain rises above 850 hPa) in two lines

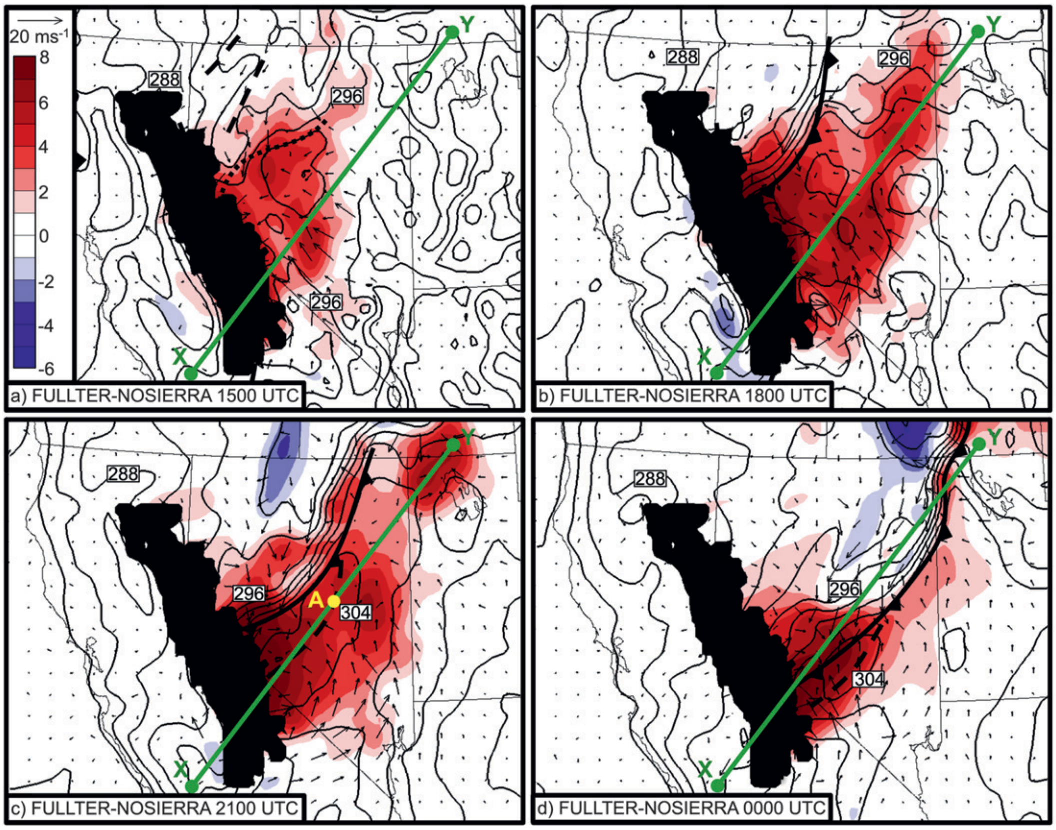

FIG. 5. FULLTER lowest half-η-level potential temperature (contours every 2 K), FULLTER–NOSIERRA lowest half-η-level potential temperature difference [K, shaded according to scale in (a)], and FULLTER–NOSIERRA lowest half-η-level vector wind difference [scale in (a)] at (a) 1500 UTC 25 Mar, (b) 1800 UTC 25 Mar, (c) 2100 UTC 25 Mar, and (d) 0000 UTC 26 Mar 2006. Region where FULLTER terrain heights exceed those of NOSIERRA is shaded black.

parallel to and downstream of the Sierra Nevada (groups Y and Z, green and light green, respectively). The FULLTER and NOSIERRA forward (backward) trajectories have the same earth-relative beginning (ending) locations.

The group X forward trajectories are diffluent in both simulations, but topographic blocking by the High Sierra leads to stronger flow splitting in FULLTER (cf. Figs. 7a and 7b). The trajectories deflected northward around the High Sierra in FULLTER partly reflect the presence of a Sierra barrier jet and the diversion of low-level Pacific air along the barrier [(e.g., Doyle 1997; Yu and Smull 2000; Neiman et al. 2002, 2004, 2010; Reeves et al. 2008), not explicitly shown]. Farther south, the pronounced blocking of low-level Pacific air is illustrated well by trajectory 5, which is deflected southward and terminates over the southern Sierra crest in FULLTER, but penetrates directly into the Intermountain West in NOSIERRA.

The FULLTER group Y and Z backward trajectories either curve around the southern periphery of the Sierra Nevada, move northward from the Mojave Desert, or traverse the High Sierra and subside in the lee (Fig. 7a). In contrast, the NOSIERRA group Y and Z trajectories penetrate directly from the Central Valley into the Intermountain West (Fig. 7b).

Changes in pressure and potential temperature along group Y and Z trajectories 1–4 (see Fig. 7 for trajectory paths and numbers) further illustrate how flow interaction with the Sierra Nevada contributes to the orographic warm anomaly development. In FULLTER, trajectories 1 and 2 begin near 700 hPa and subside abruptly in the lee of the High Sierra at ~1000 and ~0600 UTC, respectively (Fig. 8). In NOSIERRA, however, trajectories 1 and 2 begin below 900 hPa in potentially cooler low-level Pacific air, ascend over the lower windward slopes of the Sierra Nevada, and penetrate into the Intermountain West without experiencing subsidence. Since trajectories 1 and 2 experience similar net decreases in potential temperature in FULLTER and NOSIERRA, the difference in airmass origin and net vertical displacement largely accounts for the development of the northern portion of the orographic warm anomaly.

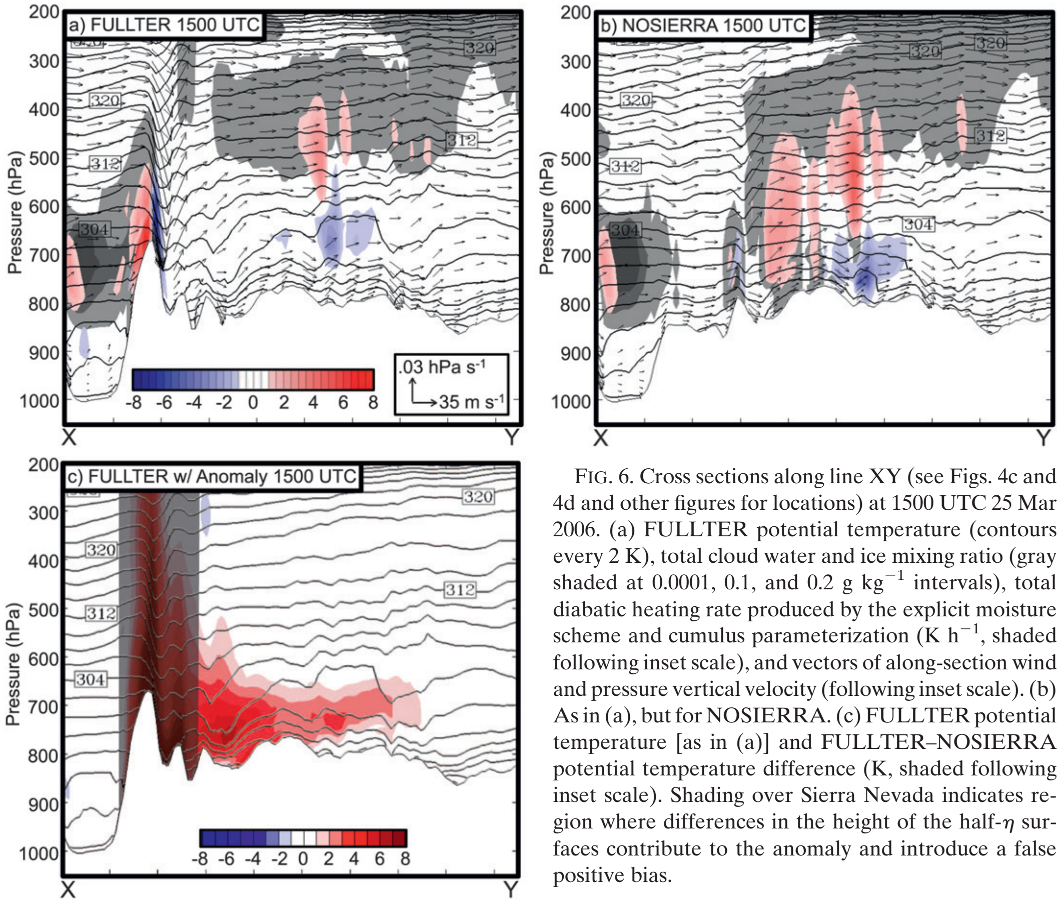

FIG. 6. Cross sections along line XY (see Figs. 4c and 4d and other figures for locations) at 1500 UTC 25 Mar 2006. (a) FULLTER potential temperature (contours every 2 K), total cloud water and ice mixing ratio (gray shaded at 0.0001, 0.1, and 0.2 g kg^{-1} intervals), total diabatic heating rate produced by the explicit moisture scheme and cumulus parameterization (K h^{-1}, shaded following inset scale), and vectors of along-section wind and pressure vertical velocity (following inset scale). (b) As in (a), but for NOSIERRA. (c) FULLTER potential temperature [as in (a)] and FULLTER–NOSIERRA potential temperature difference (K, shaded following inset scale). Shading over Sierra Nevada indicates region where differences in the height of the half-η surfaces contribute to the anomaly and introduce a false positive bias.

Nocturnal boundary layer cooling and subcloud diabatic cooling [produced by the sublimation, melting, and/or evaporation of falling precipitation (e.g., Schultz and Trapp 2003)] contribute to the decrease in potential temperature along FULLTER and NOSIERRA trajectories 1 and 2, although differences in timing and magnitude are evident (Fig. 9). FULLTER trajectories 1 and 2 avoid diabatic warming on the windward side of the High Sierra, as they cross before orographic clouds overspread the barrier. Strong gradients in horizontal wind speed, vertical velocity, and potential temperature accompanying the high-amplitude mountain wave lead to differences between the actual potential temperature change, and that derived from 15-min parameterized instantaneous heating rates in FULLTER trajectories 1 and 2.

In the southern portion of the orographic warm anomaly, FULLTER trajectories 3 and 4 originate south of the Sierra Nevada over the Mojave Desert, whereas in NOSIERRA they originate over the Central Valley of California (Fig. 7). This difference in geographic origin explains much of the development of the southern portion of the orographic warm anomaly, as the airmass over the Mojave Desert is potentially warmer than that over the Central Valley. For example, FULLTER trajectories 3 and 4 have initial potential temperatures that are 6 and 4 K higher than NOSIERRA trajectories 3 and 4, respectively (Fig. 8). Although the nocturnal boundary layer cooling is greater along FULLTER trajectories 3 and 4 than in NOSIERRA, the NOSIERRA trajectories also experience subcloud diabatic cooling (Fig. 9). The resulting differences in total potential temperature change between the two simulations are less than 1 K, indicating that differences in source region and initial potential temperature largely account for the development of the southern portion of the orographic warm anomaly.

To summarize, the initial development of the orographic warm anomaly largely reflects flow interactions with the Sierra Nevada. In FULLTER, relatively cool low-level Pacific air is largely diverted by the High Sierra, and the air that moves into the Intermountain West either subsides and adiabatically warms in their lee or originates over the Mojave Desert. In contrast, the low-level Pacific air in NOSIERRA penetrates directly into the Intermountain West. At this time, most of the orographic warm anomaly magnitude is explained by these differences in airmass origin as the trajectory-derived

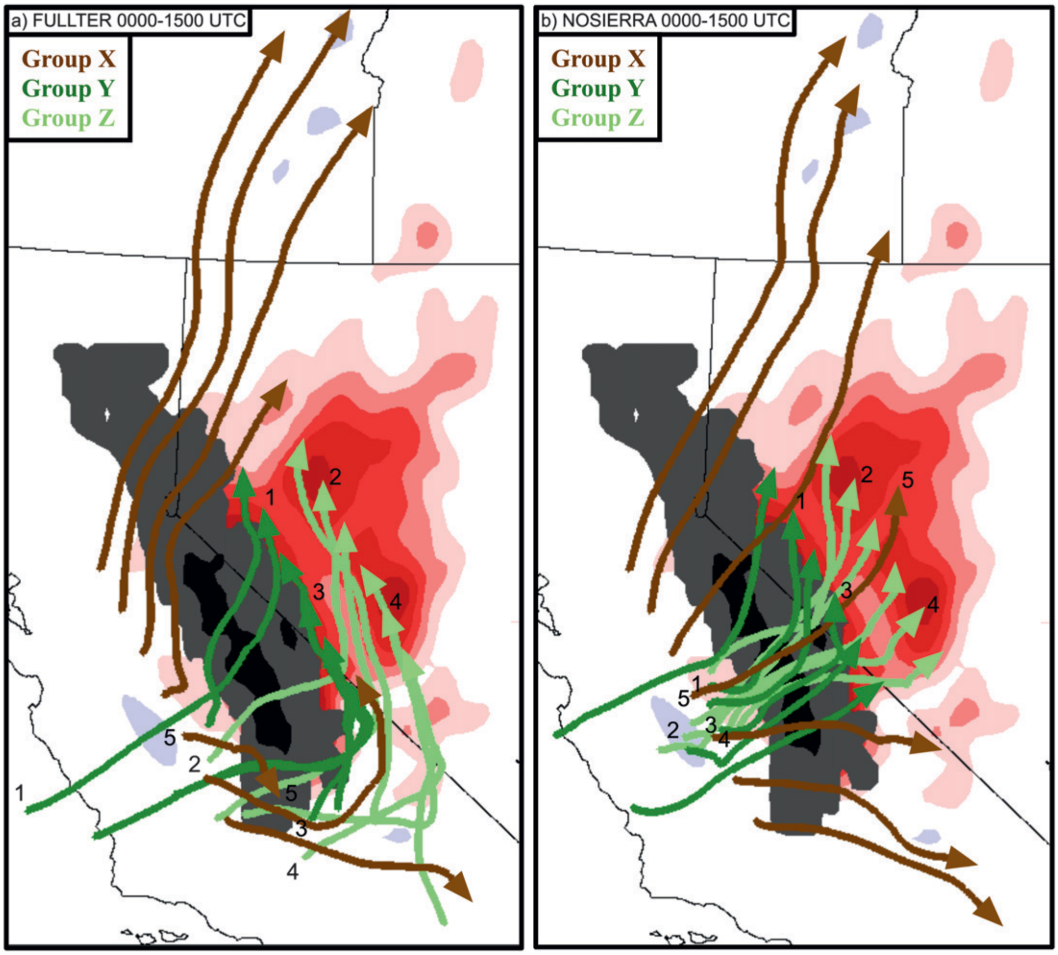

FIG. 7. Three-dimensional 15-h (0000–1500 UTC 25 Mar 2006) trajectories from (a) FULLTER and (b) NOSIERRA. Group X forward trajectories (brown) begin at 850 hPa upstream of the Sierra Nevada. Group Y and Z backward trajectories (green and light green, respectively) terminate at 850 hPa or the lowest half-η level, whichever is higher. FULLTER–NOSIERRA lowest half-η-level potential temperature difference (color filled as in Fig. 5) and terrain difference (0–1000 m, gray; >1000 m, black). Trajectory layering based on plotting order and does not indicate relative altitude. Specific trajectories discussed in text labeled to left of start position and right of ending arrow.

differences in net diabatic cooling between FULLTER and NOSIERRA are small.

c. *Frontal development*

By 1800 UTC the airstream boundary and two troughs in FULLTER merge into a single intensifying trough and cold front, whereas in NOSIERRA the nascent cold front simply forms along the solitary, preexisting trough (cf. Figs. 10a and 10b). In both simulations, a coherent kinematic frontogenesis maximum lies along the frontal zone (Figs. 10c and 10d) and the new cold front forms well in advance of the remnants of the former occluded front. Thus, discrete propagation occurs with or without the upper portion (>1500 m) of the Sierra Nevada.

Nevertheless, a larger cross-front potential temperature contrast exists in FULLTER because of the orographic warm anomaly, which has strengthened and spread across central Nevada (Fig. 5b). In contrast, there is no major postfrontal potential temperature difference between the simulations since this air mass traverses the relatively low northern Sierra Nevada and southern Cascades north of Lake Tahoe where the crest-height difference between FULLTER and NOSIERRA is <500 m (cf. Figs. 3a and 3b). Although both simulations produce postfrontal precipitation (Figs. 10a and 10b), the direct effect of diabatic frontogenesis remains relatively weak within the FULLTER frontal zone and is not coherently organized in NOSIERRA (Figs. 10e and 10f).

Cross sections from FULLTER and NOSIERRA further illustrate the influence of the High Sierra on the evolution of the orographic warm anomaly (Fig. 11). In FULLTER, a substantive orographic cloud and associated

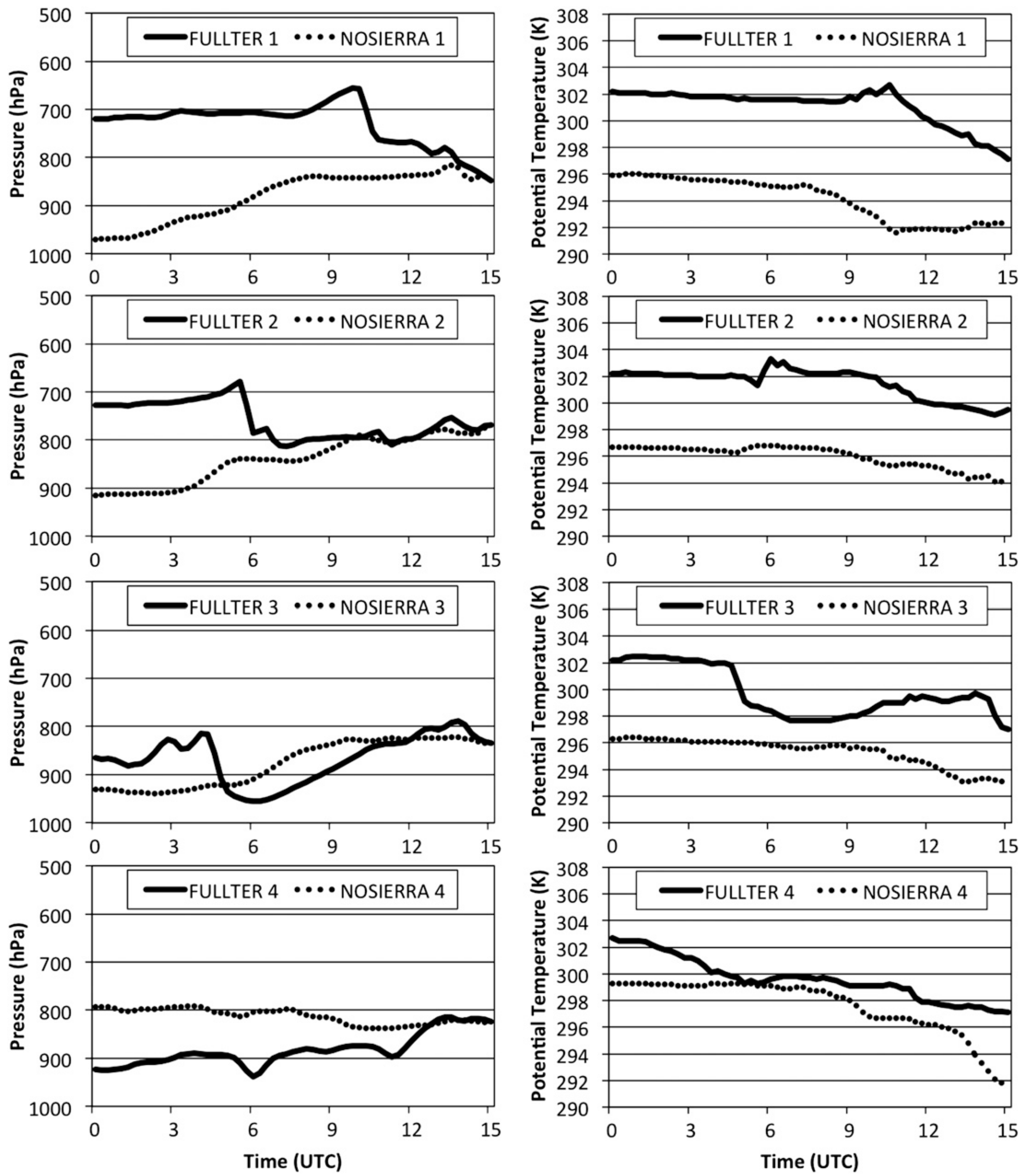

FIG. 8. (left) Pressure (hPa) and (right) potential temperature (K) along FULLTER (solid) and NOSIERRA (dashed) trajectories 1, 2, 3, and 4 of Fig. 7.

diabatic heating maximum persist over the windward slope of the Sierra Nevada, with downslope flow and a narrow region of subcloud diabatic cooling to the immediate lee (Fig. 11a). The downstream prefrontal air mass is largely cloud free with a well-mixed, ~100-hPa-deep convective boundary layer. In contrast, NOSIERRA features widespread cloud cover and precipitation within the prefrontal air mass with localized areas of subcloud diabatic cooling and a shallower convective boundary layer (Fig. 11b). Surface sensible heat fluxes are 50–150 W m^{-2} greater in FULLTER than NOSIERRA across much of the region downstream of the Sierra Nevada (Fig. 12a). These contrasts in diabatic heating and cooling, combined with advection in the southwesterly large-scale flow, contribute to the strengthening and spreading of the lower-tropospheric warm anomaly (cf. Figs. 5a, 5b, 6c, and 11c).

In both simulations a strong cold front extends across Nevada by 2100 UTC (Fig. 13). A coherent band of strong kinematic frontogenesis lies along the front (Figs. 13c and 13d). Postfrontal precipitation lags the surface cold front and the diabatic frontogenesis is generally

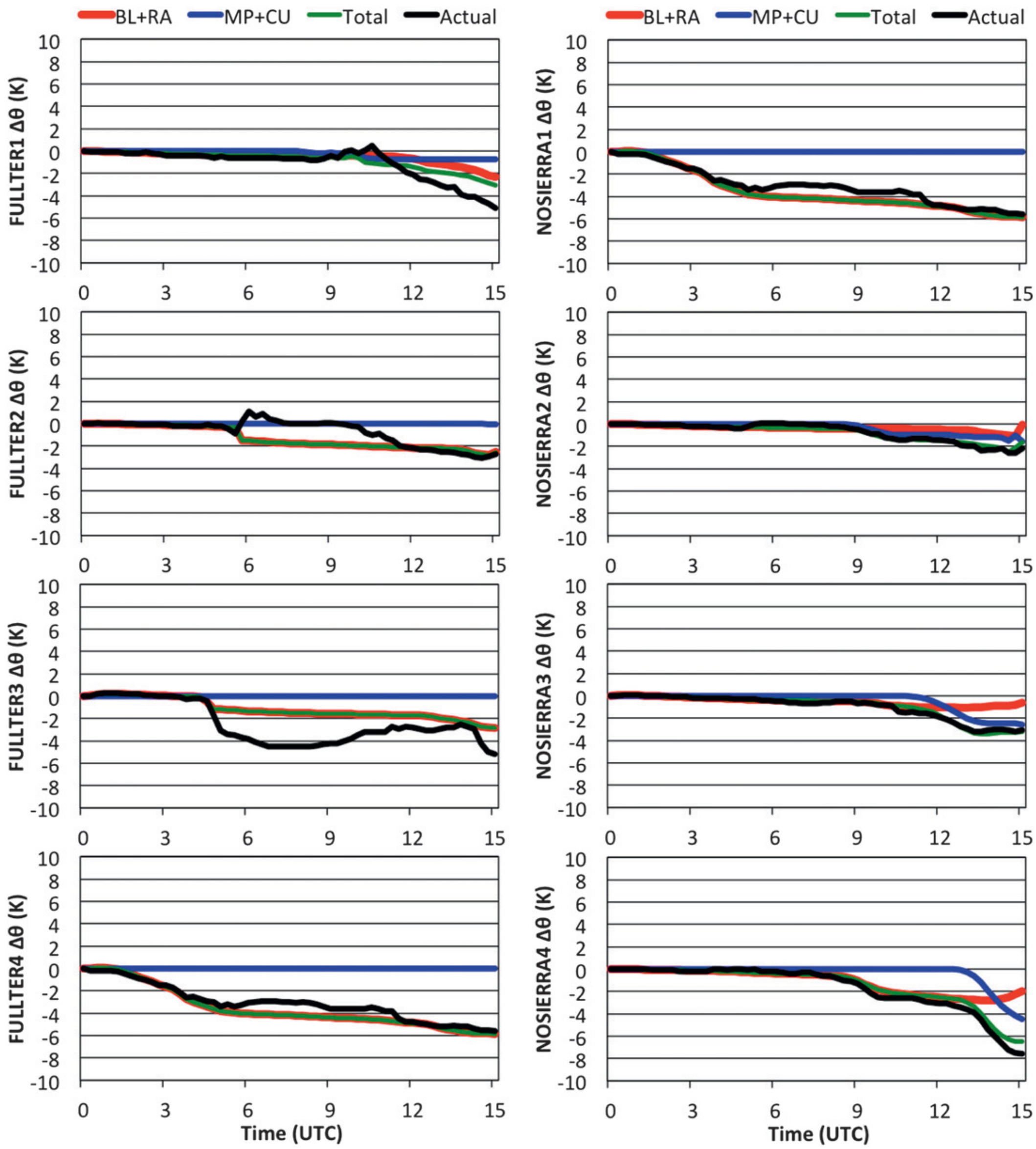

FIG. 9. Potential temperature change ($\Delta\theta$, K) along (left) FULLTER and (right) NOSIERRA trajectories 1, 2, 3, and 4 of Fig. 7. Simulation and trajectory numbers are included along the vertical-axis label. Red, blue, and green lines indicate the potential temperature change derived from temperature tendencies produced by the boundary layer and radiation parameterizations (RA+BL), microphysical and cumulus parameterizations (MP+CU), and all four parameterizations (Total), respectively. Black line indicates actual potential temperature change along trajectory.

weakly negative (i.e., frontolytical) within the frontal zone (Figs. 13e and 13f). The cross-front temperature contrast remains stronger in FULLTER due to the orographic warm anomaly, which persists in the southwesterly prefrontal flow (Figs. 5c and 14c). Prefrontal cloud cover and precipitation remain limited over the Intermountain West in FULLTER, but are widespread in NOSIERRA (cf. Figs. 13a,b and 14a,b). This leads to stronger sensible heating, a deeper convective boundary layer, and a deeper orographic warm anomaly in FULLTER (Figs. 12b and 14a–c). Soundings taken near the center of the orographic warm anomaly (point A; Figs. 5c and 13c,d) show a deeper, drier convective boundary layer and warmer prefrontal lower-tropospheric temperatures (by 3°–4°C below 700 hPa) in FULLTER compared to NOSIERRA (Fig. 15). This difference exists despite the fact that prefrontal warming in FULLTER is underdone, leading to boundary layer temperatures that are ~2°–3°C

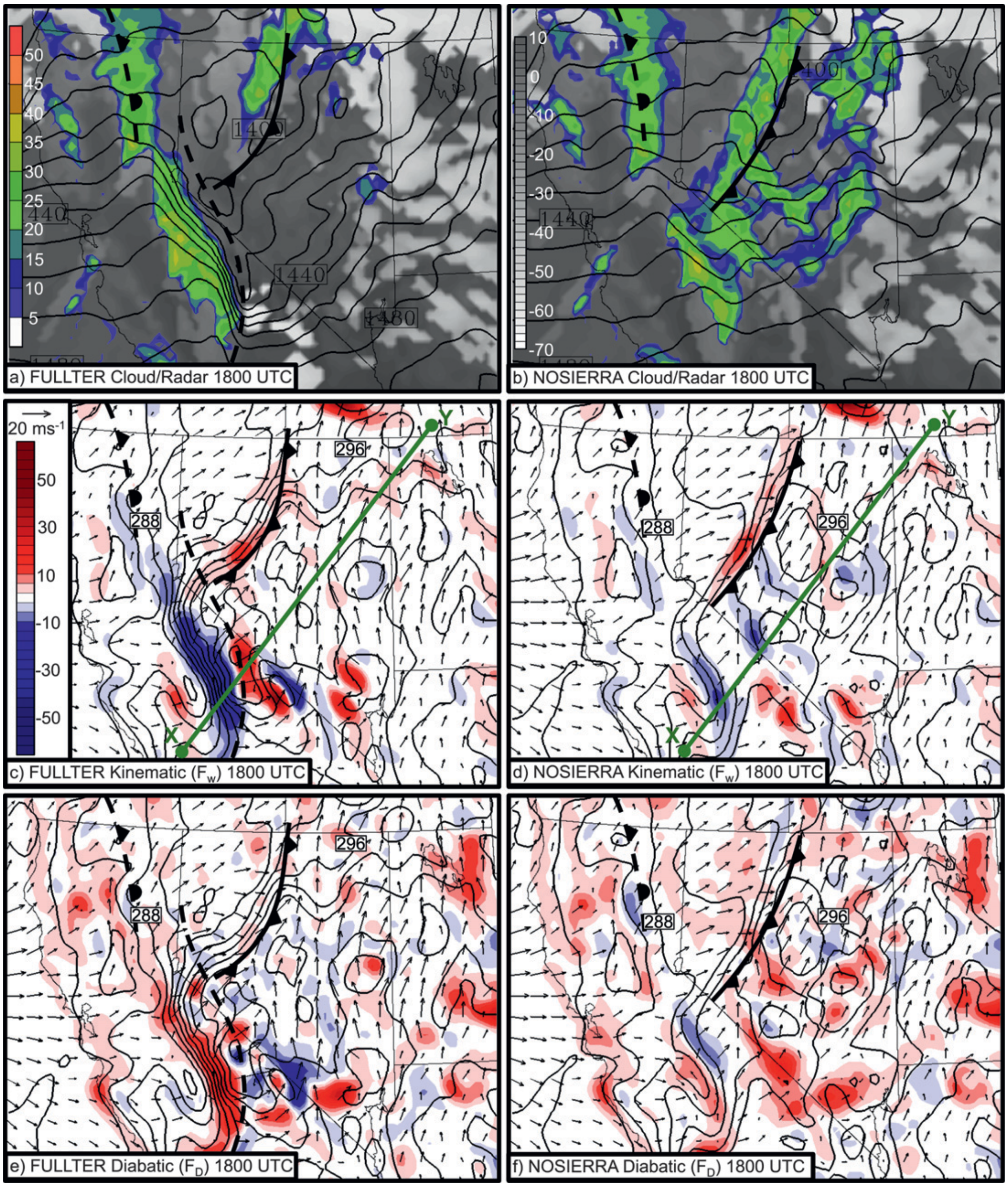

FIG. 10. As in Fig. 4, but for 1800 UTC 25 Mar 2006.

lower than observed at this time (see Steenburgh et al. 2009). Although the causes of this cold bias remain unknown, these results, combined with the trajectory analysis below, suggest that diabatic processes over and to the lee of the Sierra Nevada are one possible error source.

d. Trajectory analysis of the orographic warm anomaly and cold front at 2100 UTC

Nine-hour three-dimensional backward trajectories that begin at 1200 UTC and end at 2100 UTC provide a Lagrangian perspective on the development of the mature orographic warm anomaly and Intermountain cold front (Fig. 16). A dense grid of trajectories encompassing the FULLTER and NOSIERRA cold fronts was examined, but for clarity we present a grid that is one-fourth as dense, with trajectories grouped based upon ending location and trajectory history. FULLTER and NOSIERRA trajectories with corresponding numbers have the same earth-relative termination point at 2100 UTC on the lowest half-η level.

Group A trajectories in both simulations (Fig. 16, dark blue) originate over north-central California, cross the

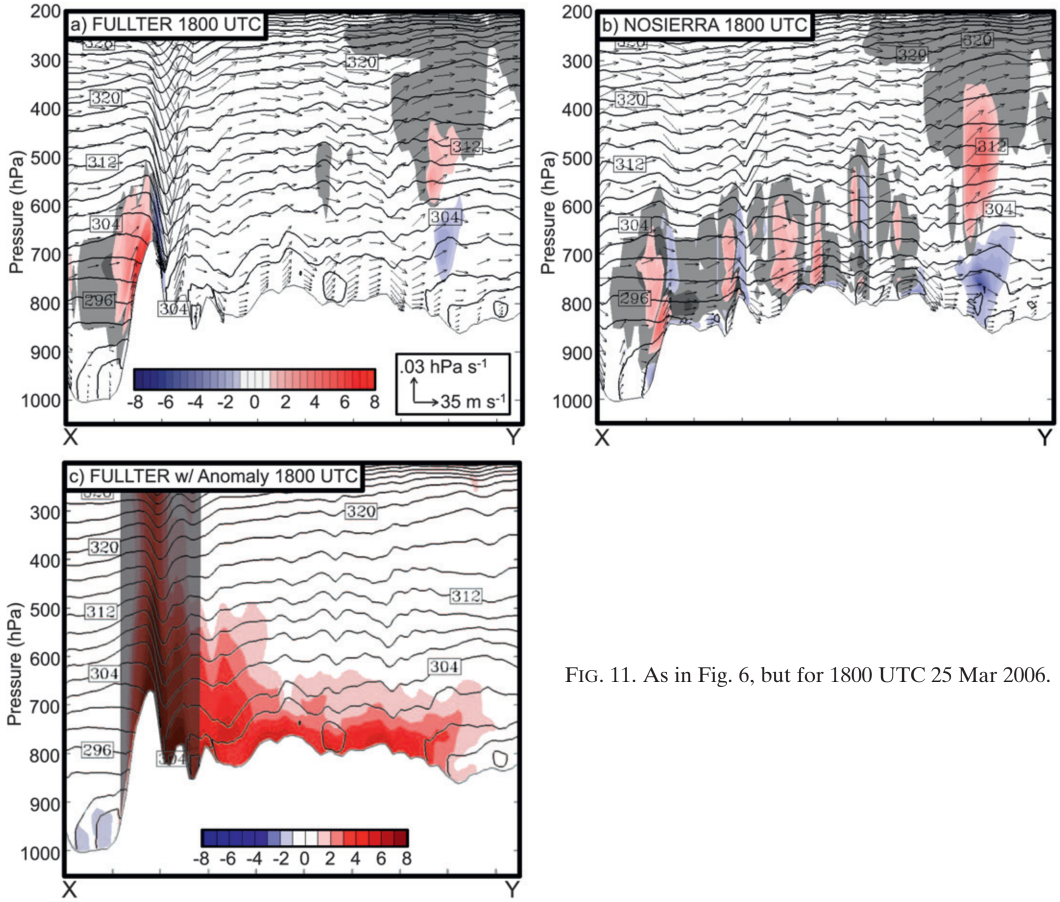

FIG. 11. As in Fig. 6, but for 1800 UTC 25 Mar 2006.

northern Sierra Nevada, and terminate in the postfrontal air mass over northwest Nevada. Compared with NOSIERRA, the FULLTER trajectories that terminate immediately behind the front are influenced by a stronger frontal trough, experience greater deflection, and have a stronger front-relative component (cf. Figs. 16a and 16b). Most FULLTER and NOSIERRA trajectories that terminate at a common location have similar beginning and ending pressures and potential temperatures (e.g., trajectory A2; Fig. 17). Further, similar amounts of daytime boundary layer heating occur along these trajectories, with secondary local diabatic contributions as trajectories move through areas of precipitation and cloud (e.g., trajectory A2; Fig. 18).

Group B trajectories in both simulations (Fig. 16, light blue) originate near the southern periphery of the Sierra Nevada and terminate within the prefrontal air mass over southern and central Nevada. The FULLTER group B trajectories, however, experience greater deflection around the southern periphery of the High Sierra (cf. Figs. 16a and 16b). The FULLTER group B trajectories also have a stronger front-relative component over the Intermountain West, consistent with the stronger lee and frontal troughs (see also Fig. 5c). On average the FULLTER group B trajectories have an ending potential temperature that is 3.5 K higher than those in NOSIERRA, with diabatic processes playing an important role in this contrast. Trajectory B23, for example, begins with a lower potential temperature and higher initial pressure in FULLTER than NOSIERRA, but terminates with a potential temperature that is 6 K higher (Fig. 17). This results from a lack of subcloud diabatic cooling, combined with stronger boundary layer heating (Fig. 18). Thus, the lack of diabatic cooling from precipitation and increased sensible heating within the cloud and precipitation shadow contribute to the development and strengthening of the orographic warm anomaly along these trajectories.

The FULLTER group C trajectories (Fig. 16a, magenta) originate near the Pacific coast, are forced up the windward slopes of the High Sierra, and experience diabatic heating and a loss of water content within the orographic cloud (i.e., airmass transformation). They then descend rapidly into the lee of the High Sierra where they experience boundary layer heating. For example, FULLTER trajectory C18 begins at ~900 hPa, ascends

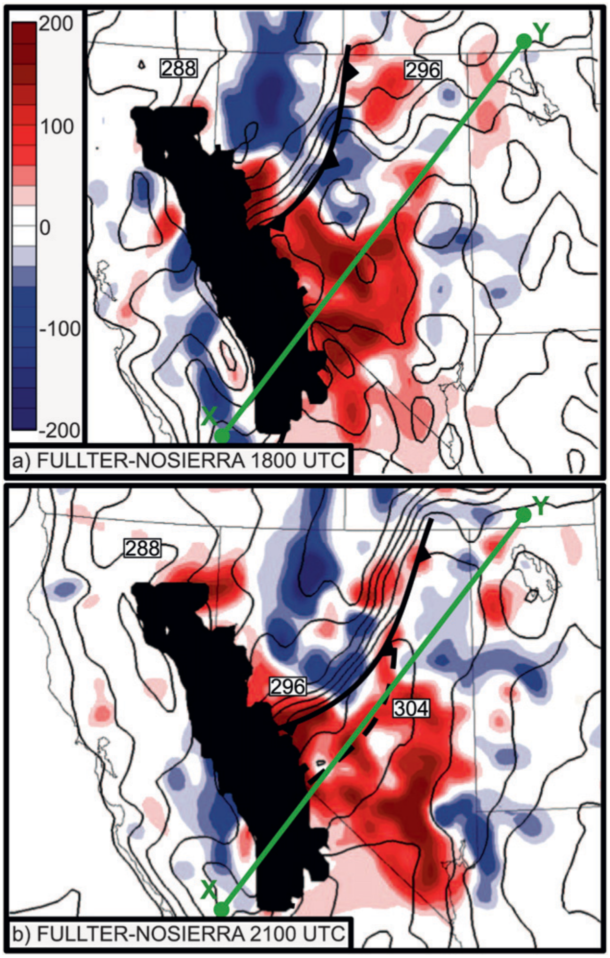

FIG. 12. FULLTER lowest half-η-level potential temperature (contours every 2 K) and FULLTER–NOSIERRA surface heat flux difference [W m^{-2}, shaded according to scale in (a)] at (a) 1800 UTC 25 Mar and (b) 2100 UTC 25 Mar 2006.

to ~725 hPa over the windward slopes of the High Sierra, and then descends to ~800 hPa in their lee (Fig. 17). The potential temperature along this trajectory increases ~8 K due to diabatic heating within the orographic cloud and then ~6 K due to subsequent boundary heating downstream of the High Sierra (Figs. 17 and 18). In contrast, NOSIERRA trajectory C18 begins at 850 hPa with a potential temperature that is ~3 K higher, but experiences a net potential temperature increase of only ~2 K, terminating with a potential temperature that is ~7 K lower than in FULLTER (Fig. 17). The NOSIERRA trajectory C18 crosses the Sierra Nevada through a large gap in the orographic precipitation region (see also Fig. 13b), and thus does not experience diabatic heating over the windward slopes of the Sierra Nevada, but does experience weak boundary layer heating (Fig. 18). In the lee it experiences cooling from precipitation and continued weak boundary layer heating.

The FULLTER group D trajectories (Fig. 16a, yellow) originate over the lower Colorado River basin and terminate in the prefrontal air mass over eastern Nevada. In NOSIERRA, the southernmost group D trajectories (21, 25, 29, and 32) are similar to those in FULLTER with comparable tracks and small beginning and ending potential temperature differences (Fig. 16b, potential temperature not shown). The northernmost group D trajectories (6, 11, 16, and 20), however, originate over southern Nevada. The difference in the origin of the northernmost FULLTER and NOSIERRA group D trajectories reflects the stronger frontal and lee troughs in FULLTER, which causes stronger, meridionally oriented flow, especially early in the trajectory lifetime. In addition, FULLTER group D northernmost trajectories experience greater diabatic heating than those in NOSIERRA. For example, the net increase in potential temperature along FULLTER trajectory D16 is ~7 K compared to ~1 K along NOSIERRA trajectory D16 (Fig. 17). Most of this difference is explained by cooling from precipitation in NOSIERRA (Fig. 18), which largely counters daytime boundary layer heating and does not occur in FULLTER due to cloud and precipitation shadowing downstream of the Sierra Nevada.

The FULLTER group E trajectories originate near the southern periphery of the Sierra Nevada, whereas the NOSIERRA group E trajectories originate in potentially cooler air to the north (Figs. 16a and 16b, purple). For example, FULLTER trajectory E12 begins with an initial pressure that is comparable to NOSIERRA, but the potential temperature is about 3 K higher (Fig. 17). This largely explains the difference in the ending potential temperatures between the two trajectories since both experience similar cooling as they move through an area of precipitation between 1600 and 1800 UTC and boundary layer warming thereafter (Fig. 18).

To summarize, the High Sierra profoundly affect the regional flow, with several processes contributing to the orographic warm anomaly evolution from 1200 to 2100 UTC. The High Sierra largely block the penetration of low-level Pacific air into the Intermountain West. Parcels that are able to surmount the High Sierra undergo dramatic airmass transformation (i.e., diabatic heating and loss of water content in the orographic cloud) and subside into the lee (e.g., trajectory C18). The High Sierra also lead to stronger, more meridional flow from the Mojave Desert and lower Colorado River basin into the Intermountain West. The cloud and precipitation shadow downstream of the range results in greater daytime boundary layer heating and reduced cooling from precipitation. The contribution of boundary layer heating is likely maximized in this event because the cold front develops and moves across Nevada during the daytime.

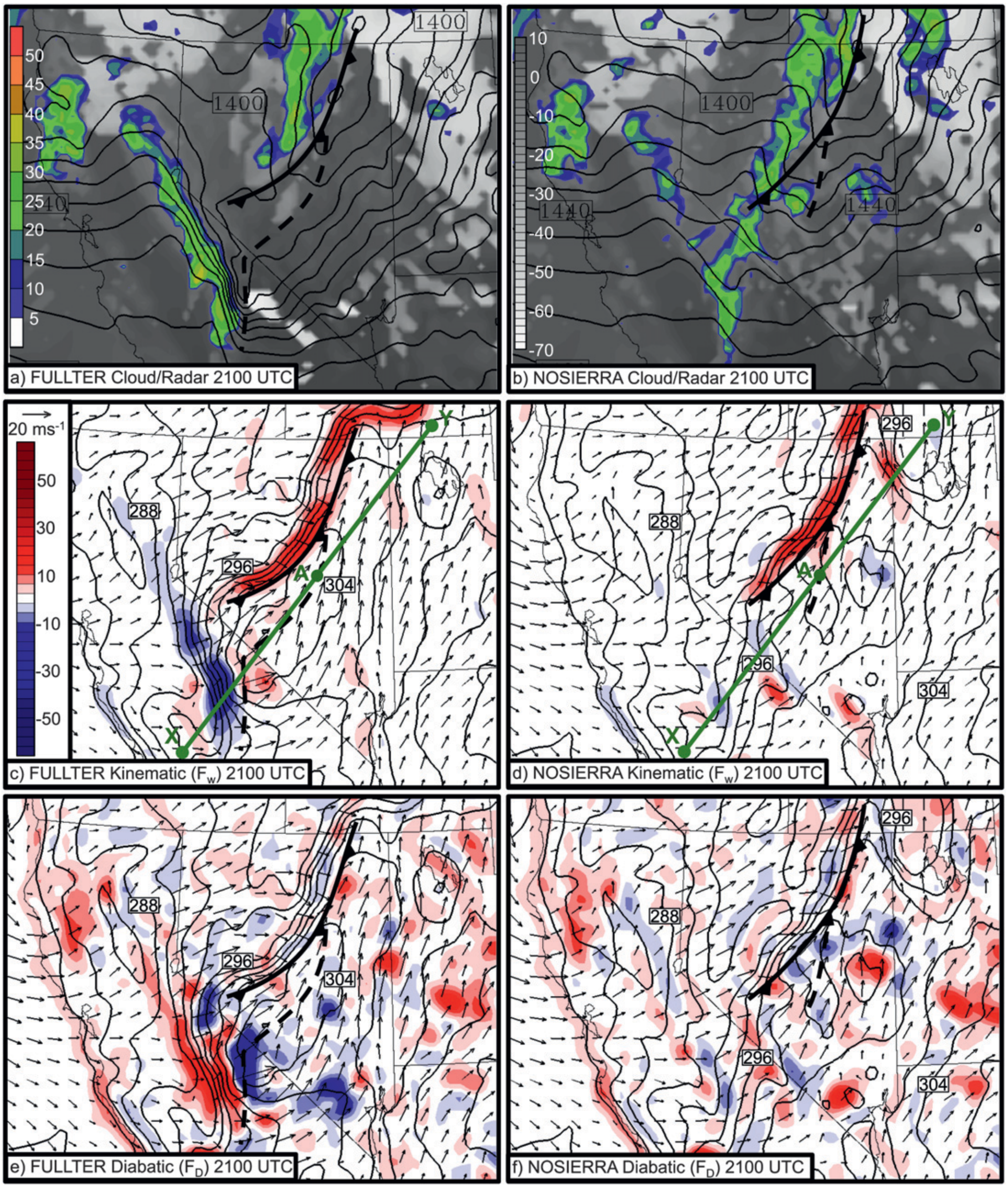

FIG. 13. As in Fig. 4, but for 2100 UTC 25 Mar 2006.

In contrast, orographic modification of the postfrontal air mass is quite limited.

e. Frontal strength over eastern Nevada

In both simulations, the cold front strengthens through 0000 UTC 26 March (Figs. 19c and 19d) as the postfrontal precipitation band phases with the surface front (Figs. 19a and 19b), and the prefrontal convective boundary layer becomes fully developed [not explicitly shown; see Steenburgh et al. (2009)]. During this period, kinematic (Figs. 19c and 19d) and diabatic frontogenesis (Figs. 19e and 19f) become stronger and better organized in FULLTER than in NOSIERRA, leading to a stronger front. In particular, the magnitude of the surface potential temperature gradient (i.e., $|\nabla_\eta \theta|$) is ~25% larger in FULLTER than NOSIERRA (cf. Figs. 20a and 20b). Although the orographic warm anomaly is strongest directly downstream of the High Sierra where cold air has encircled the southern end of the barrier forming a seclusion of warm air in FULLTER, a neck of the orographic warm anomaly persists just ahead of the front (Fig. 5d). Farther downstream of the Sierra Nevada,

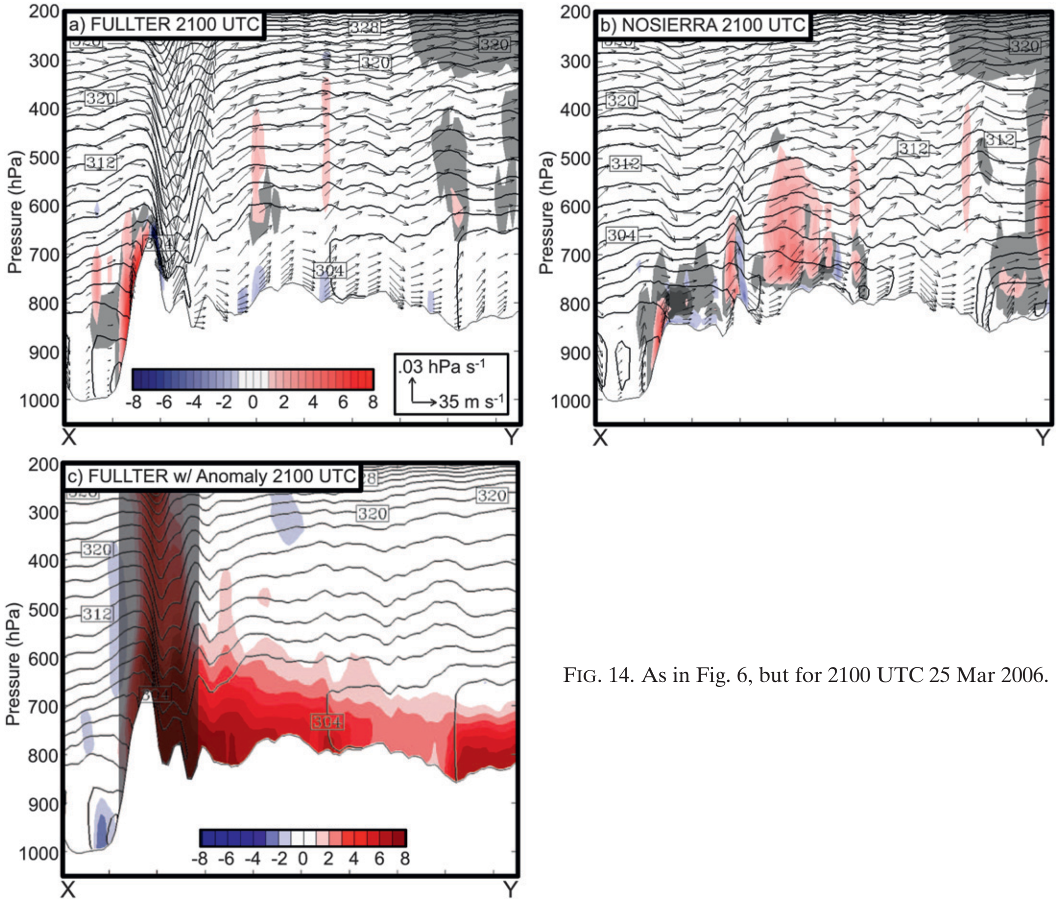

FIG. 14. As in Fig. 6, but for 2100 UTC 25 Mar 2006.

the cold front moves into the plane of cross-section XY in both simulations (cf. Figs. 19c,d and 21a,b). As this occurs, the orographic warm anomaly ascends into the middle and upper troposphere and is removed from the surface (Fig. 21c).

The presence of the High Sierra leads to stronger frontal development (as inferred from the magnitude of the lowest half-η-level potential temperature gradient; cf. Figs. 20a and 20b) in the full-physics runs (FULLTER versus NOSIERRA; cf. Figs. 20a and 20b) as well as in FKDRY simulations that do not include the diabatic effects of cloud and precipitation processes (cf. Figs. 20c and 20d). Thus, the stronger FULLTER front does not simply reflect more intense subcloud diabatic cooling in the postfrontal environment.

Ageostrophic circulations are essential for frontal development, especially on such rapid time scales (<12 h), and result from geostrophic adjustment as large-scale deformation concentrates a horizontal temperature gradient (Hoskins and Bretherton 1972). In some cases, frontal development may be enhanced by terrain-induced flows (Volkert et al. 1991; Colle et al. 1999; Steenburgh and Blazek 2001), differential subcloud diabatic cooling (Schultz and Trapp 2003), and/or differential surface heating (e.g., Koch et al. 1995, 1997; Gallus and Segal 1999, Sanders 1999; Segal et al. 2004).

For the 25 March 2006 cold front, terrain-induced flows appear to play the greatest role in the immediate lee of the Sierra Nevada where the pressure trough in FULLTER is much stronger than that found in NOSIERRA (cf. Figs. 13a and 13b). This results in enhanced front-relative flow in the prefrontal and postfrontal environments (Fig. 5c), with the resulting deformation and convergence producing a front that is much stronger in FULLTER than NOSIERRA (cf. Figs. 20a and 20b).

Subcloud diabatic cooling contributes to frontal development in areas more removed from the Sierra Nevada (i.e., over northern Nevada), where a pronounced postfrontal precipitation band develops in both simulations. In this region, simulations that do not include the diabatic effects of cloud and precipitation processes (FULLTER-FKDRY and NOSIERRA-FKDRY) produce weaker frontal temperature gradients than their full-physics counterparts (cf. Figs. 20a,c and 20b,d). The related cooling in the postfrontal environment is larger in FULLTER than NOSIERRA (Figs. 5c and 5d), which,

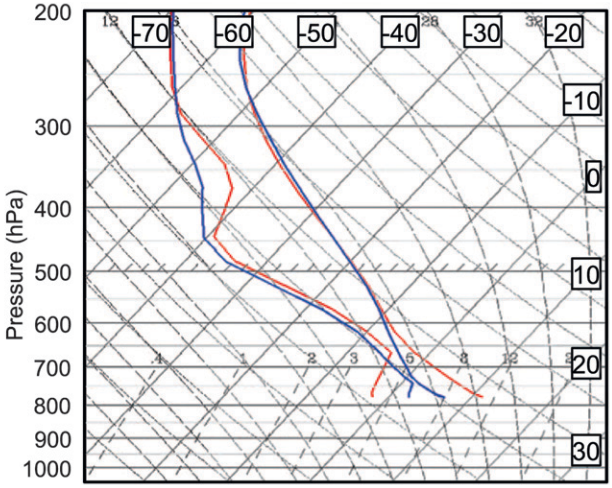

FIG. 15. FULLTER (red) and NOSIERRA (blue) skew T–log$p$ diagram (temperature and dewpoint) for point A (see Figs. 5c and 13c,d for location) at 2100 UTC 25 Mar 2006.

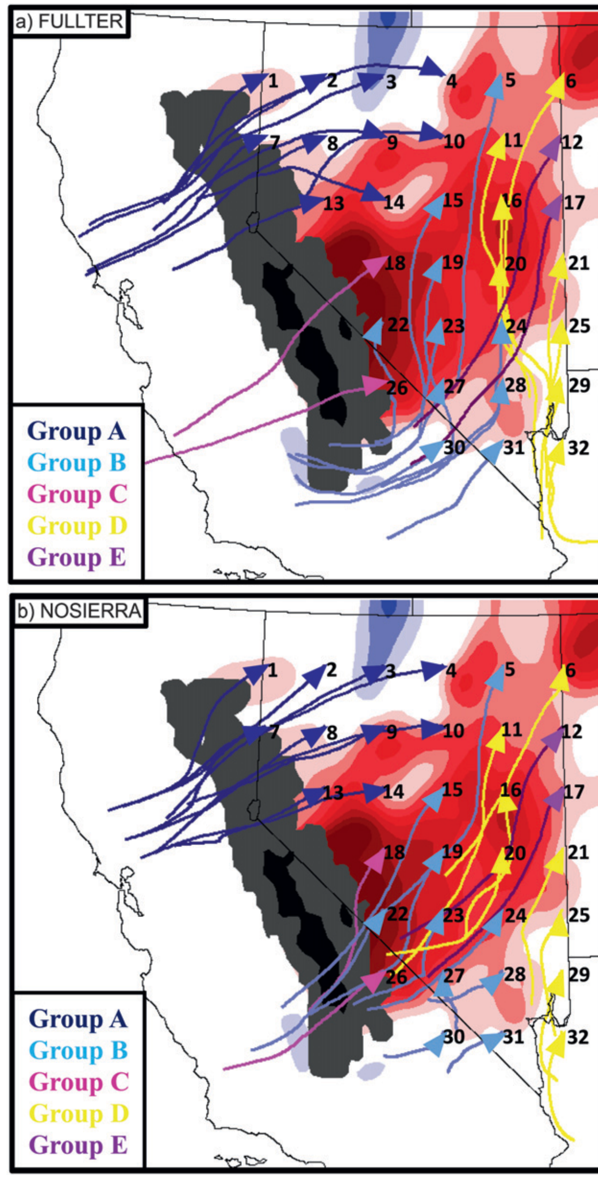

FIG. 16. Three-dimensional 9-h (1200–2100 UTC 25 Mar 2006) backward trajectories from (a) FULLTER and (b) NOSIERRA. Trajectory groups color coded following inset at lower left. FULLTER–NOSIERRA lowest half-η-level potential temperature difference (color filled as in Fig. 5) and terrain difference (0–1000 m, gray; >1000 m, black). Trajectory layering based on plotting order and does not indicate relative altitude. FULLTER and NOSIERRA trajectories with corresponding numbers have the same earth-relative termination point at 2100 UTC on the lowest half-η level.

combined with the reduced prefrontal cloud and precipitation, suggests that the indirect influence of the Sierra Nevada is to enhance the differential diabatic cooling and its influence on frontal development in this case.

Finally, the frontal development is strongly influenced by boundary layer heating of the prefrontal environment, which is greater in FULLTER because of the cloud and precipitation shadow downstream of the High Sierra. Although this ultimately contributes to stronger diabatic frontogenesis in FULLTER compared to NOSIERRA (cf. Figs. 19e and 19f), it likely also contributes to the stronger kinematic frontogenesis since differential heating arising from inhomogeneous cloud cover is known to generate a thermally forced circulation that enhances the cross-front ageostrophic circulation (e.g., Koch et al. 1995, 1997; Gallus and Segal 1999; Segal et al. 2004). Thus, the influence of the Sierra Nevada on this event extends beyond their direct influence on wind and temperature and includes their indirect downstream influences on clouds, precipitation, sensible heating, and subsequent frontal intensification.

4. Conclusions

Recent studies show that the Intermountain West is a common breeding ground for strong, rapidly developing cold fronts. Numerical simulations of the 25 March 2006 Intermountain cold front described here illustrate one way that the Sierra Nevada can enhance cold-front development, contributing to the high frequency of strong cold-frontal passages over the Intermountain West. Specifically, a comparison of a full-terrain simulation (FULLTER) with one in which the height of the Sierra Nevada and southern Cascades of California is restricted to no more than 1500 m (NOSIERRA) shows that the interaction of southwesterly flow with the formidable southern High Sierra creates a prefrontal orographic warm anomaly that enhances the cross-front temperature contrast. Several processes generate this orographic warm anomaly.

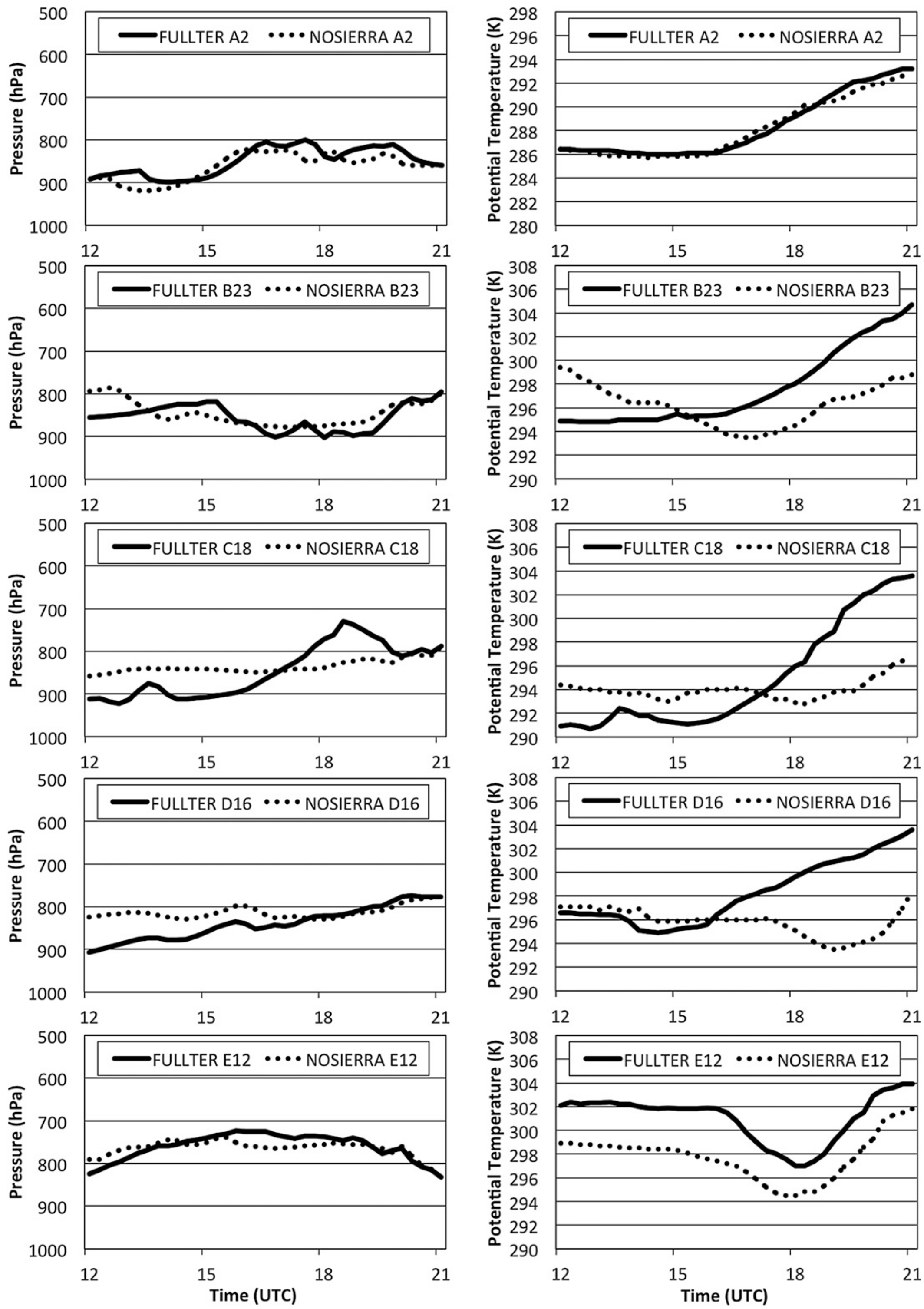

FIG. 17. As in Fig. 8, but for selected trajectories in Fig. 16. Note unique potential temperature scale in upper-right graph.

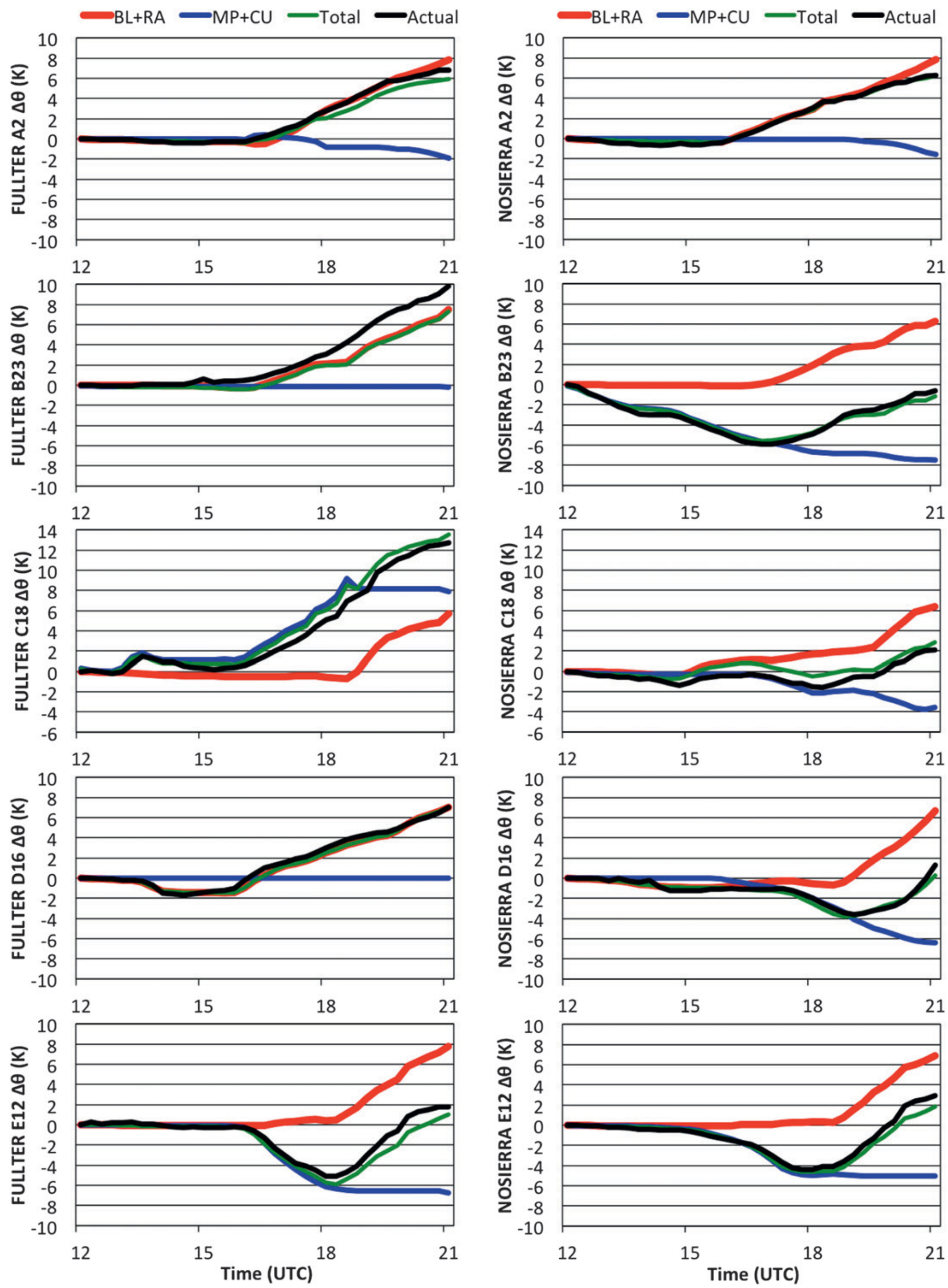

FIG. 18. As in Fig. 9, but for selected trajectories of Fig. 16 and group letter also included along the vertical-axis label. Note unique $\Delta\theta$ scale in middle (trajectory C18) graphs.

First, the High Sierra modify the regional flow by blocking low-level Pacific air, creating leeward subsidence, and enhancing southerly flow from the Mojave Desert and lower Colorado River basin into the Intermountain West. Second, diabatic heating and water content loss occur in areas of orographic precipitation, warming and drying parcels that traverse the High Sierra crest and move into the lee. Finally, there is increased daytime boundary layer

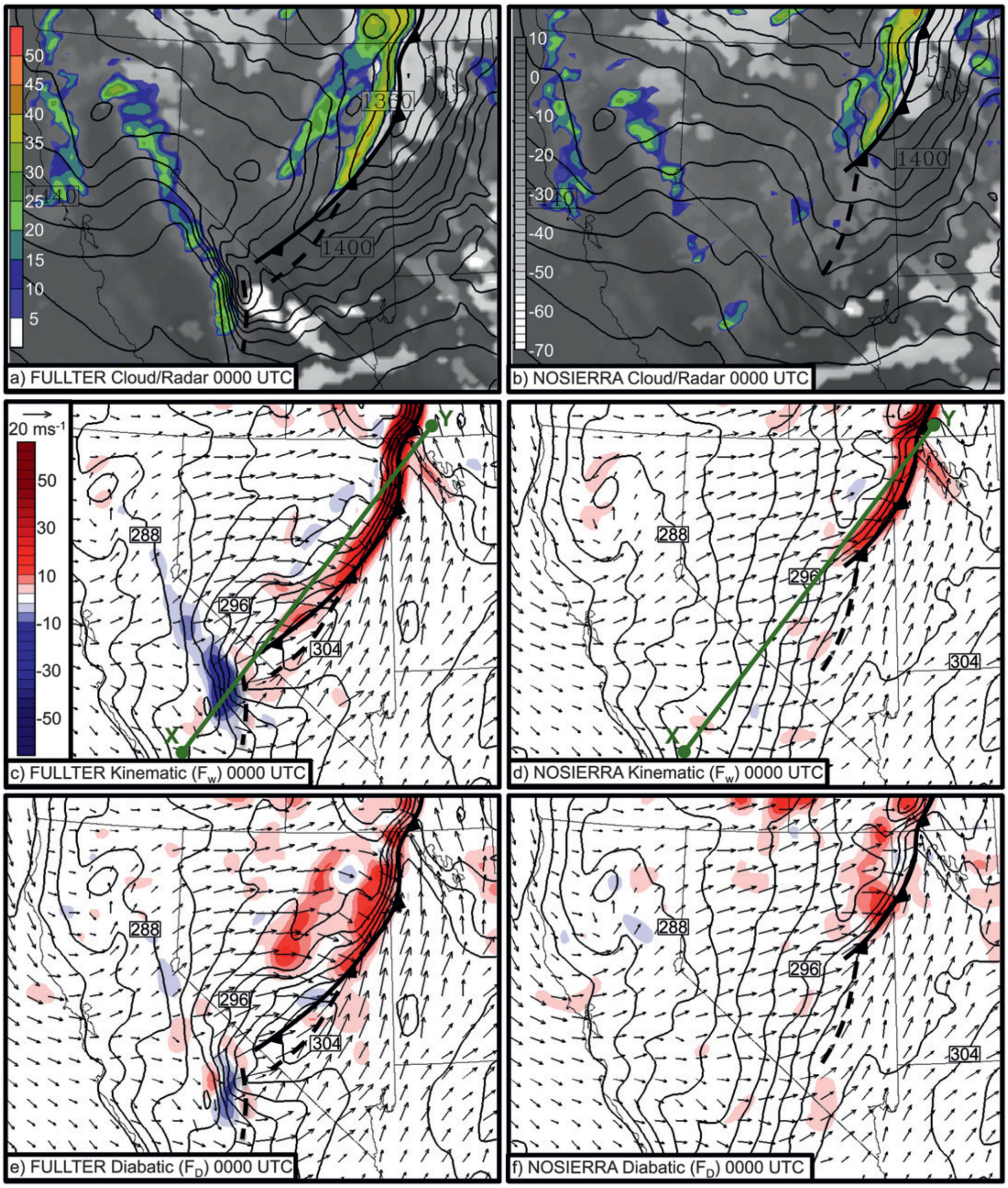

FIG. 19. As in Fig. 4, but for 0000 UTC 26 Mar 2006.

heating and reduced subcloud diabatic cooling within the downstream cloud and precipitation shadow. Flow modification is primarily responsible for the initial formation of the anomaly, while the diabatic processes become important later in the event during the cold-front development. Collectively, these orographic effects lead to a stronger front, but have little influence on the frontal movement, including the discrete propagation across the Sierra–Cascade ranges and western Nevada. Nevertheless, these results illustrate that the Sierra Nevada can enhance frontal development and may contribute to the high frequency of strong cold-frontal passages over the Intermountain West.

As shown in Shafer and Steenburgh (2008), strong Intermountain cold fronts occur most frequently in the late spring (April–June), and in the late afternoon and evening (maximum at 1800 LST), indicating the importance of daytime heating. The role of prefrontal sensible heating within the downstream cloud and precipitation shadow is likely maximized in this event since the front develops and moves across Nevada during the day. Such heating would not occur at night, when radiative cooling

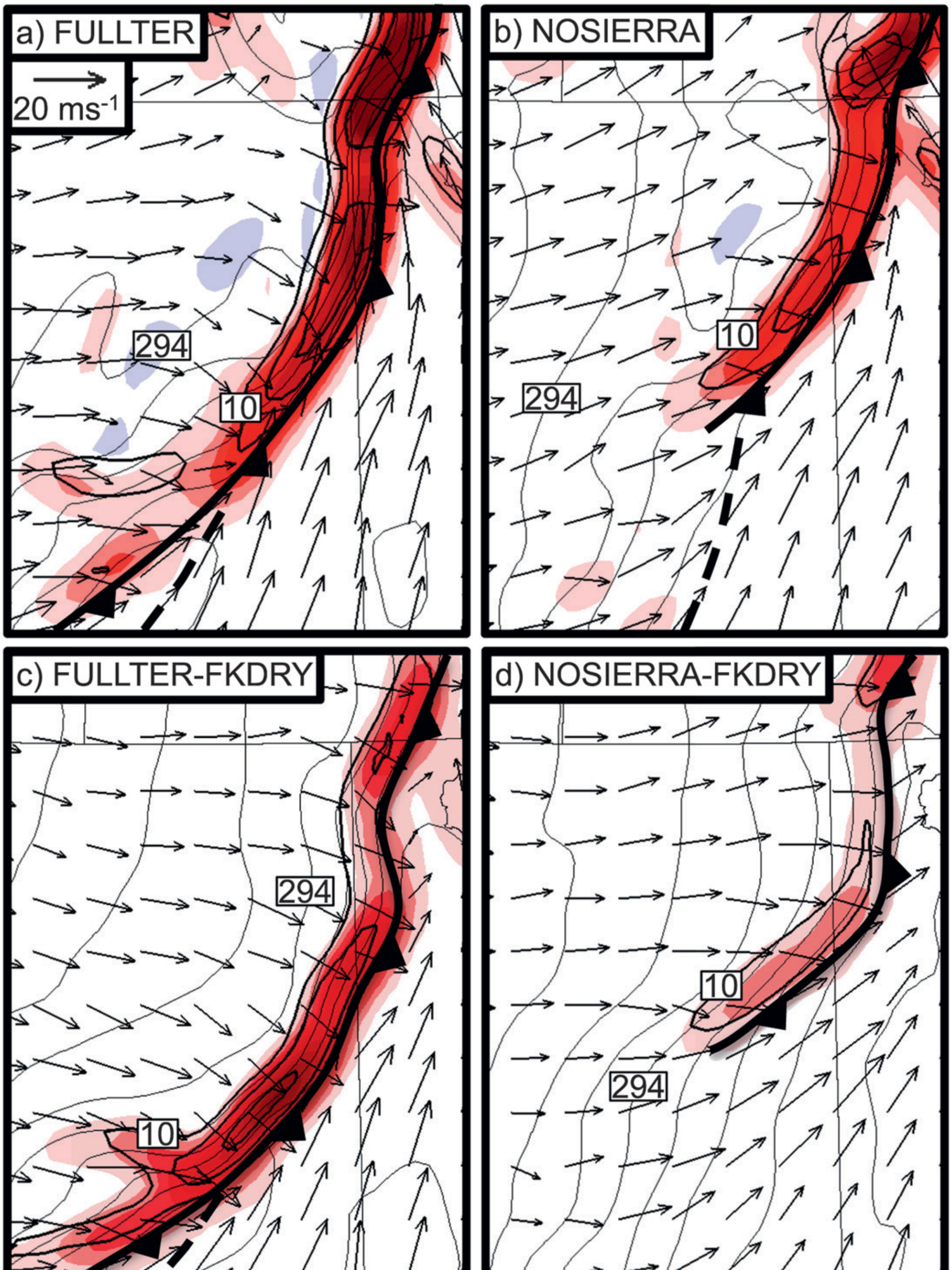

FIG. 20. Lowest half-η-level potential temperature (thin contours every 2 K), potential temperature gradient magnitude [thick contours every 5 K $(100\ \mathrm{km})^{-1}$ beginning with 10 K $(100\ \mathrm{km})^{-1}$], wind [vector scale at upper left of (a)], and kinematic frontogenesis [K $(100\ \mathrm{km\ h})^{-1}$, shaded following scale in Fig. 4c] from (a) FULLTER, (b) NOSIERRA, (c) FULLTER–FKDRY, and (d) NOSIERRA–FKDRY at 0000 UTC 26 Mar 2006.

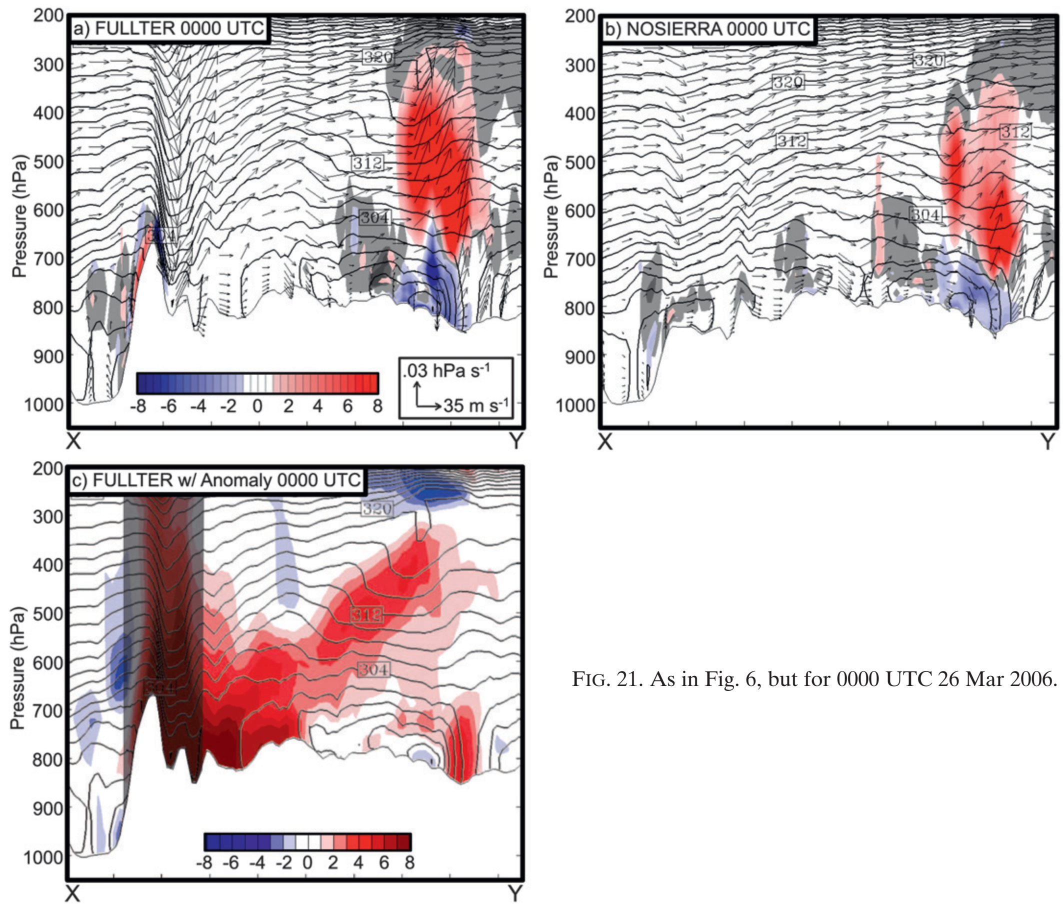

FIG. 21. As in Fig. 6, but for 0000 UTC 26 Mar 2006.

might reduce the strength of the prefrontal orographic warm anomaly and potentially contribute to frontolysis.

Although the discrete propagation and rapid cold-front development observed during this event were generally well simulated by FULLTER, prefrontal warming was underdone and the front moved across western Nevada about 2–3 h too early (Steenburgh et al. 2009). The results presented here suggest that the prefrontal cold bias could be related to inadequate simulation of processes responsible for creating the orographic warm anomaly. While proper representation and simulation of these processes could be important for accurate surface sensible weather forecasts during similar events, the similarity in frontal positioning between FULLTER, NOSIERRA, and the FKDRY simulations suggests that errors in the timing of frontal passages may be more strongly influenced by large-scale processes than orographic processes associated with the High Sierra.

This study adds to our growing understanding of the influence of the Sierra Nevada on the Intermountain cyclone and front evolution. One underlying issue, however, is determining the mechanisms responsible for the development of troughing and confluence over northern Nevada, which frequently occurs during Intermountain cold-front events (e.g., Shafer and Steenburgh 2008; Steenburgh et al. 2009; West and Steenburgh 2010). Shafer and Steenburgh (2008) and Steenburgh et al. (2009) suggest that this confluence, which lies downstream of the Sierra Nevada, might be terrain enhanced. Further, West and Steenburgh (2010) show how a similar confluence zone, which they call the Great Basin confluence zone (GBCZ), formed downstream of the Sierra Nevada and served as the locus for frontogenesis and cyclogenesis during the 2002 Tax Day Storm. Although the NOSIERRA sensitivity study presented here illustrates that the High Sierra enhance frontal development, it also shows that downstream confluence and cold-front development occur even in their absence. Further work is needed to better understand the development of confluence downstream of the Sierra Nevada and its role in frontal evolution over the Intermountain West.

Acknowledgments. We thank Trevor Alcott, Lance Bosart, Larry Dunn, John Horel, Jan Paegle, David Schultz, Ed Zipser, and three anonymous reviewers for their suggestions and comments, and gratefully acknowledge the provision of datasets, software, or computer time and services by NCEP, NCAR, Unidata, the Center for Ocean–Land–Atmosphere Studies, and the University of Utah Center for High Performance Computing. This research was supported by National Science Foundation Grant ATM-0627937 and the National Weather Service C-STAR program. Any opinions, findings, and conclusions or recommendations expressed in this material are those of the authors and do not necessarily reflect the views of the National Science Foundation or the National Weather Service.

REFERENCES

Barnes, S. L., F. Caracena, and A. Marroquin, 1996: Extracting synoptic-scale diagnostic information from mesoscale models: The Eta Model, gravity waves, and quasigeostrophic diagnostics. *Bull. Amer. Meteor. Soc.,* **77,** 519–528.

Braun, S. A., R. A. Houze Jr., and B. F. Smull, 1997: Airborne dual-Doppler observations of an intense frontal system approaching the Pacific Northwest coast. *Mon. Wea. Rev.,* **125,** 3131–3156.

Chen, F., and J. Dudhia, 2001: Coupling an advanced land surface–hydrology model with the Penn State–NCAR MM5 Modeling System. Part I: Model implementation and sensitivity. *Mon. Wea. Rev.,* **129,** 569–585.

Colle, B. A., C. F. Mass, and B. F. Smull, 1999: An observational and numerical study of a cold front interacting with the Olympic Mountains during COAST IOP5. *Mon. Wea. Rev.,* **127,** 1310–1334.

——, B. F. Smull, and M.-J. Yang, 2002: Numerical simulations of a landfalling cold front observed during COAST: Rapid evolution and responsible mechanisms. *Mon. Wea. Rev.,* **130,** 1945–1966.

Doyle, J. D., 1997: The influence of mesoscale orography on a coastal jet and rainband. *Mon. Wea. Rev.,* **125,** 1465–1488.

Dudhia, J., 1989: Numerical study of convection observed during the Winter Monsoon Experiment using a mesoscale two-dimensional model. *J. Atmos. Sci.,* **46,** 3077–3107.

Galewsky, J., and A. Sobel, 2005: Moist dynamics and orographic precipitation in northern and central California during the New Year's flood of 1997. *Mon. Wea. Rev.,* **133,** 1594–1612.

Gallus, W. A., Jr., and M. Segal, 1999: Diabatic effects on late-winter cold front evolution: Conceptual and numerical model evaluations. *Mon. Wea. Rev.,* **127,** 1518–1537.

Giorgi, F., and G. T. Bates, 1989: The climatological skill of a regional model over complex terrain. *Mon. Wea. Rev.,* **117,** 2325–2347.

Hoinka, K. P., and H. Volkert, 1992: Fronts and the Alps: Findings from the Front Experiment. *Meteor. Atmos. Phys.,* **48,** 51–75.

Hoskins, B. J., and F. P. Bretherton, 1972: Atmospheric frontogenesis models: Mathematical formulation and solution. *J. Atmos. Sci.,* **29,** 11–37.

Janjić, Z. I., 2002: Nonsingular implementation of the Mellor–Yamada level 2.5 scheme in the NCEP Meso Model. NCEP Office Note 437, 61 pp.

Jiang, Q., and J. D. Doyle, 2008: Diurnal variation of downslope winds in Owens Valley during the Sierra Rotor Experiment. *Mon. Wea. Rev.,* **136,** 3760–3780.

Kain, J. S., and J. M. Fritsch, 1990: A one-dimensional entraining/detraining plume model and its application in convective parameterization. *J. Atmos. Sci.,* **47,** 2784–2802.

——, and ——, 1993: Convective parameterization for mesoscale models: The Kain–Fritsch scheme. *The Representation of Cumulus Convection in Numerical Models, Meteor. Monogr.,* No. 46, Amer. Meteor. Soc., 165–170.

Koch, S. E., J. T. McQueen, and V. M. Karyampudi, 1995: A numerical study of the effects of differential cloud cover on cold frontal structure and dynamics. *J. Atmos. Sci.,* **52,** 937–964.

——, A. Aksakal, and J. T. McQueen, 1997: The influence of mesoscale humidity and evapotranspiration fields on a model forecast of a cold-frontal squall line. *Mon. Wea. Rev.,* **125,** 385–409.

Kurz, M., 1990: The influence of the Alps on the structure and behaviour of cold fronts over southern Germany. *Meteor. Atmos. Phys.,* **43,** 61–68.

Lee, T. F., 1987: Seasonal and interannual trends of Sierra Nevada clouds and precipitation. *J. Climate Appl. Meteor.,* **26,** 1270–1276.

Lundquist, J. D., J. R. Minder, P. J. Neiman, and E. Sukovich, 2010: Relationships between barrier jet heights, orographic precipitation gradients, and streamflow in the northern Sierra Nevada. *J. Hydrometeor.,* **11,** 1141–1156.

Mellor, G. L., and T. Yamada, 1982: Development of a turbulence closure model for geophysical fluid problems. *Rev. Geophys. Space Phys.,* **20,** 851–875.

Miller, J. E., 1948: On the concept of frontogenesis. *J. Meteor.,* **5,** 169–171.

Mlawer, E. J., S. J. Taubman, P. D. Brown, M. J. Iacono, and S. A. Clough, 1997: Radiative transfer for inhomogeneous atmosphere: RRTM, a validated correlated-k model for the longwave. *J. Geophys. Res.,* **102** (D14), 16 663–16 682.

Neiman, P. J., F. M. Ralph, R. L. Weber, T. Uttal, L. B. Nance, and D. H. Levinson, 2001: Observations of nonclassical frontal propagation and frontally forced gravity waves adjacent to steep topography. *Mon. Wea. Rev.,* **129,** 2633–2659.

——, ——, A. B. White, D. E. Kingsmill, and P. O. G. Persson, 2002: The statistical relationship between upslope flow and rainfall in California's Coastal Mountains: Observations during CALJET. *Mon. Wea. Rev.,* **130,** 1468–1492.

——, ——, P. O. G. Persson, A. B. White, D. P. Jorgensen, and D. E. Kingsmill, 2004: Modification of fronts and precipitation by coastal blocking during an intense landfalling winter storm in southern California: Observations during CALJET. *Mon. Wea. Rev.,* **132,** 242–273.

——, E. M. Sukovich, F. M. Ralph, and M. Hughes, 2010: A seven-year wind profiler–based climatology of the windward barrier jet along California's northern Sierra Nevada. *Mon. Wea. Rev.,* **138,** 1206–1233.

Petterssen, S., 1936: Contribution to the theory of frontogenesis. *Geofys. Publ.,* **11** (6), 1–27.

——, 1956: *Motion and Motion Systems*. Vol. 1, *Weather Analysis and Forecasting,* 2nd ed. McGraw-Hill, 428 pp.

Rauber, R. M., 1992: Microphysical structure and evolution of a central Sierra Nevada orographic cloud system. *J. Appl. Meteor.,* **31,** 3–24.

Reeves, H. D., Y.-L. Lin, and R. Rotunno, 2008: Dynamic forcing and mesoscale variability of heavy precipitation events over the Sierra Nevada mountains. *Mon. Wea. Rev.,* **136,** 62–77.

Sanders, F., 1999: A short-lived cold front in the southwestern United States. *Mon. Wea. Rev.,* **127,** 2395–2403.

Schultz, D. M., and R. J. Trapp, 2003: Nonclassical cold-frontal structure caused by dry subcloud air in northern Utah during the Intermountain Precipitation Experiment (IPEX). *Mon. Wea. Rev.,* **131,** 2222–2246.

Seaman, N. L., 1987: Program TRAJEC: Documentation and users guide. PSU-NWPLIB-0010-87, 95 pp.

Segal, M., E. A. Aligo, and W. A. Gallus Jr., 2004: A conceptual and scaling evaluation of the surface wetness effect on daytime moisture convergence along a surface cold front with differential cloud cover. *J. Hydrometeor.,* **5,** 365–371.

Shafer, J. C., and W. J. Steenburgh, 2008: Climatology of strong Intermountain cold fronts. *Mon. Wea. Rev.,* **136,** 784–807.

——, ——, J. A. W. Cox, and J. P. Monteverdi, 2006: Terrain influences on synoptic storm structure and mesoscale precipitation distribution during IPEX IOP3. *Mon. Wea. Rev.,* **134,** 478–497.

Shapiro, M. A., 1984: Meteorological tower measurements of a surface cold front. *Mon. Wea. Rev.,* **112,** 1634–1639.

Sinclair, M. R., 1994: A diagnostic model for estimating orographic precipitation. *J. Appl. Meteor.,* **33,** 1163–1175.

Skamarock, W. C., J. B. Klemp, J. Dudhia, D. O. Gill, D. M. Barker, W. Wang, and J. G. Powers, 2005: A description of the Advanced Research WRF version 2. NCAR Tech. Note 5, 22 pp.

Smith, B. L., S. E. Yuter, P. J. Neiman, and D. E. Kingsmill, 2010: Water vapor fluxes and orographic precipitation over northern California associated with a landfalling atmospheric river. *Mon. Wea. Rev.,* **138,** 74–100.

Smith, G. I., I. Friedman, H. Klieforth, and K. Hardcastle, 1979: Areal distribution of deuterium in eastern California precipitation, 1968–1969. *J. Appl. Meteor.,* **18,** 172–188.

Smith, R. B., Q. Jiang, M. G. Fearon, P. Tabary, M. Dorninger, J. D. Doyle, and R. Benoit, 2003: Orographic precipitation and air mass transformation: An Alpine example. *Quart. J. Roy. Meteor. Soc.,* **129,** 433–454.

——, I. Barstad, and L. Bonneau, 2005: Orographic precipitation and Oregon's climate transition. *J. Atmos. Sci.,* **62,** 177–191.

Steenburgh, W. J., and T. R. Blazek, 2001: Topographic distortion of a cold front over the Snake River plain and central Idaho mountains. *Wea. Forecasting,* **16,** 301–314.

——, C. R. Neuman, G. L. West, and L. F. Bosart, 2009: Discrete frontal propagation over the Sierra–Cascade mountains and Intermountain West. *Mon. Wea. Rev.,* **137,** 2000–2020.

Thompson, G., R. M. Rasmussen, and K. Manning, 2004: Explicit forecasts of winter precipitation using an improved bulk microphysics scheme. Part I: Description and sensitivity analysis. *Mon. Wea. Rev.,* **132,** 519–542.

——, P. R. Field, W. D. Hall, and R. M. Rasmussen, 2006: A new bulk microphysical parameterization for WRF & MM5. Preprints, *Seventh Weather Research and Forecasting User's Workshop,* Boulder, CO, NCAR, 5.3.

Varney, B. M., 1920: Monthly variations of the precipitation–altitude relation in the central Sierra Nevada of California. *Mon. Wea. Rev.,* **48,** 648–650.

Volkert, H., L. Weickmann, and A. Tafferner, 1991: The Papal front of 3 May 1987: A remarkable example of frontogenesis near the Alps. *Quart. J. Roy. Meteor. Soc.,* **117,** 125–150.

West, G. L., and W. J. Steenburgh, 2010: Life cycle and mesoscale frontal structure of an Intermountain cyclone. *Mon. Wea. Rev.,* **138,** 2528–2545.

Yu, C.-K., and B. F. Smull, 2000: Airborne Doppler observations of a landfalling cold front upstream of steep coastal orography. *Mon. Wea. Rev.,* **128,** 1577–1603.